

BAYERISCHE JULIUS-MAXIMILIANS-UNIVERSITÄT WÜRZBURG
FAKULTÄT FÜR PHYSIK UND ASTRONOMIE
LEHRSTUHL FÜR ASTRONOMIE



BACHELOR'S THESIS

Four Years of TANAMI VLBI
observations of the unusual γ -ray
source PMN J1603–4904

Author: Amar Hekalo
Supervisor: Prof. Dr. Matthias Kadler
Submission date: December 10, 2015

Zusammenfassung

In dieser Arbeit werden die Ergebnisse der Analyse neuer Daten des aktiven Galaxienkerns (AGN) PMN J1603–4904 präsentiert und diskutiert. AGN sind leuchtstarke, extragalaktische Quellen, die Licht des gesamten elektromagnetischen Spektrum emittieren. Beobachtungen von AGN weisen ähnliche Eigenschaften von Gruppen an Quellen auf, was zu einem Klassifizierungssystem und einem Modell zur Vereinheitlichung führt. Einige AGN Klassen emittieren Materieströme aus dem Kern, welche als Jets bezeichnet werden. Es ist nicht viel über die Prozesse bekannt, welche zur Entstehung von Jets führen. Diese können nur durch hochauflösende Beobachtungen untersucht werden.

Very Long Baseline Interferometrie (VLBI) ist zur Zeit die einzige Methode, mit welcher ausreichende Auflösungen erreicht werden, um die Radioemissionen von AGN auf (Sub-)Parsecskalen zu beobachten und die detaillierte Struktur von Jets zu untersuchen. VLBI nutzt die Eigenschaften der Fourier Transformation und kombiniert Teleskope weltweit zu einem Array. Dies erreicht Auflösungen, welche mit Einzelteleskopen nicht realisierbar sind. Diese Methode erlaubt es, intrinsische Eigenschaften von Jets zu untersuchen, wie ihrer Geschwindigkeit und Winkel zur Sichtlinie.

Das TANAMI (Tracking Active Galactic Nuclei with Austral Milliarcsecond Interferometry) Programm ist ein VLBI Monitoring Programm, dessen Zweck die Beobachtung extragalaktischer γ -Strahlungsquellen südlich einer Deklination von -30° bei Frequenzen von 8.4 GHz und 22.3 GHz ist. VLBI Daten werden mit Daten anderer Beobachtungsprogramme kombiniert, um die Multiwellenlängeneigenschaften von AGN Jets zu untersuchen. PMN J1603–4904 gehört zum TANAMI sample, welches 75 der hellsten extragalaktischen Jets am Südhimmel beinhaltet.

Es wurden mit Daten zweier neuer VLBI Epochen von PMN J1603–4904 Images erstellt und im Kontext früherer Beobachtungen analysiert. Die Quelle ist als BL Lac Objekt klassifiziert. Bisherige Ergebnisse weisen zwei verschiedene Rotverschiebungen von $z = 0.18 \pm 0.01$ und $z = 0.2321 \pm 0.0004$ auf. Die kleinskalige Struktur stellt diese Klassifizierung in Frage, weshalb weitere Untersuchungen mit VLBI Beobachtungen nötig sind.

Die Images und Modelle sind vereinbar mit den bereits vorhandenen Epochen. Die Quelle weist eine Struktur aus drei Komponenten mit einem hellen Zentrum auf, wie man es bei Compact Symmetric Objects (CSO) sieht. Die kinematische Analyse liefert keine besonderen Variabilitäten der Struktur, Strahlungsflussdichte sowie Helligkeitstemperatur. Ebenso kann keine signifikante Bewegung festgestellt werden. Die Obergrenze für die Jetgeschwindigkeit wird zu $|v_{\text{app}}| < 0.11 \text{ mas/yr}$, was $\beta_{\text{app}} < 1.8$ bei $z = 0.2321$ entspricht, berechnet, was eine signifikante Verbesserung zu früheren Ergeb-

nissen darstellt.

Es wird ein weiteres Modell mit mehr als drei Komponenten erstellt und die Konsistenz für alle Epochen verifiziert. Die resultierenden Eigenschaften aus der kinematischen Analyse stimmen mit dem einfachen Modell überein, weshalb das neue Modell die gleiche Gesamtstruktur darstellt, aber kleinräumige Strukturen detaillierter wiedergibt. Auch hier kann keine signifikante Bewegung festgestellt werden.

Die Klassifizierung von PMN J1603–4904 wird diskutiert. Eine Klassifizierung als CSO ist wahrscheinlich, es wäre aber die erste Quelle dieses Typs mit starker Emission von γ -Strahlung.

Abstract

In this thesis the results of analysis of new data on the unusual AGN PMN J1603–4904 are presented and discussed. Active Galactic Nuclei (AGN) are highly luminous cores of distant galaxies that emit light across the entire electromagnetic spectrum. AGN observations reveal similar properties for groups of sources, leading to a system of classification and further a single model of unification. Some AGN types display emission of matter in a jet-like structure directly from the core. Not much is known about the origin and creation processes of jets and can only be investigated by high resolution observations.

Very Long Baseline Interferometry (VLBI) is currently the only method able to achieve sufficient resolutions to observe the radio emission of AGN on (sub-)parsec scales, revealing the detailed structure of jets. VLBI utilizes the properties of Fourier transformation and combines telescopes across the globe to one array which achieves resolutions that are impossible to realize with a single-dish telescope. This technique enables the measurement of intrinsic jet properties, such as its speed and inclination angle.

The TANAMI (Tracking Active Galactic Nuclei with Austral Milliarcsecond Interferometry) program is a VLBI monitoring program set to observe and monitor extragalactic γ -ray sources south of a declination of -30° at frequencies of 8.4 GHz and 22.3 GHz. VLBI data is combined with data from other observation programs to investigate the multiwavelength properties of AGN jets. PMN J1603–4904 is part of the TANAMI sample containing 75 of the brightest extragalactic jets on the southern hemisphere.

Two new VLBI epochs of PMN J1603–4904 were imaged and analyzed within the context of past observations. The source is classified as a BL Lac object. Previous results present two different redshifts of $z = 0.18 \pm 0.01$ and $z = 0.2321 \pm 0.0004$. The mas-scale structure challenges this classification, leading to the necessity of further investigations with VLBI observations.

The final images and models are consistent with previous data, resulting in a three component structure with a bright center, typical for a Compact Symmetric Object (CSO). The kinematic analysis yields no notable variabilities in structure, flux density and brightness temperature. No significant motion could be detected. However an upper limit to the apparent jet speed of $|v_{\text{app}}| < 0.11 \text{ mas/yr}$, corresponding to $\beta_{\text{app}} < 1.8$ at $z = 0.2321$, is determined, which is a significant improvement over past results.

Another model containing several more components is developed and verified to be consistent within all epochs. The properties found with kinematic analysis are consistent with the simple model, hence this model is said to describe the same structures, but only in more detail. Again no significant motion nor variability is detected.

The classification of PMN J1603–4904 is discussed. The source is likely to be classified as a CSO, but would be the first source of this type to display strong γ -ray emission.

Contents

Zusammenfassung	i
Abstract	iii
1 Scientific Background	3
1.1 Active Galactic Nuclei	3
1.1.1 Classification and unification	3
1.1.2 Emission processes in jets	6
1.1.3 Brightness temperature	8
1.1.4 Relativistic boosting and jet kinematics	8
1.2 Very Long Baseline Interferometry	11
1.2.1 Theory of VLBI	11
1.2.2 Analyzing VLBI data	14
1.2.3 TANAMI	15
1.3 Previous results	17
1.3.1 Measured redshifts	17
1.3.2 Multiwavelength properties	19
2 TANAMI VLBI Observations of PMN J1603–4904 in 2012 and 2013	23
2.1 Imaging and modelfitting	23
2.2 Kinematic analysis	27
2.3 Complex modelfitting	31
3 Discussion	37
3.1 Orientation and kinematics of the jet system	37
3.2 Implications for the classification of PMN J1603–4904	39
4 Summary and Outlook	41
Acknowledgments	43
Bibliography	45

1 Scientific Background

1.1 Active Galactic Nuclei

Active Galactic Nuclei (AGN) are among the brightest sources in the sky. They are classified as active when their emission cannot be attributed to stellar emission by the host galaxy, i.e. thermal emission by stars, but instead stems from non-thermal broadband emission.

The core is generally highly luminous compared to the host galaxy with luminosities ranging from 10^{42} to $10^{48} \frac{\text{erg}}{\text{s}}$. This luminosity is powered by a supermassive black hole (SMBH) at the center of an AGN's host galaxy which assembles an accretion disk of surrounding dust material by gravitational pull. The gravitational energy released in this process is enough to reach the given luminosities (see e.g. Kembhavi and Narlika, 1999).

The electromagnetic spectrum abides by a power law indicating non-thermal emission. Depending on the type of AGN emission lines can appear allowing to measure their distance by determining the Doppler shift. Additionally AGN show large variability in their luminosity across the entire spectrum on time scales from hours to years.

Some AGN display emission of a jet from the core which can be detected on all wavelengths. These jets move at highly relativistic speeds, often seemingly multiple times larger than the speed of light which can be explained by projectional effects. This phenomenon is named superluminal motion. Additionally relativistic jets undergo Doppler boosting (see Sect. 1.1.4), appearing brighter/fainter when moving towards/away from an observer. In many cases, these jets end in large radio lobes.

There are still many questions remaining about AGN and their jets, such as the origin and formation processes of jets, what they are made of and what processes lead to the measured emission. The answers to these questions are fundamental to the understanding of AGN physics, so there are many reasons to keep AGN observations going.

The following sections will give brief explanations on the classification of AGN and some physical properties like the underlying emission processes in jets.

1.1.1 Classification and unification

Multiwavelength observation of many AGN show a large variety in their broadband emission leading to the conclusion that they can be assigned to different classes depending on their specific properties. There are various approaches on how to classify these galaxies

focusing on different features and characteristics. Here I will focus on the characteristics of BL Lac objects and radio galaxies, specifically their younger versions, while shortly mentioning the other classes. For more details see e.g. Kembhavi and Narlika (1999).

A first classification, following Kellermann, Sramek, et al. (1989), roughly divides all AGN into two groups, *radio loud* and *radio quiet* ones. This is done by taking the ratio R_{r-o} of their radio flux density S_r and optical flux density S_o : $R_{r-o} = \frac{S_r}{S_o}$. An AGN is considered radio loud if $R_{r-o} > 10$ and radio quiet if $0.1 < R_{r-o} < 10$. The majority of AGN are radio quiet, where only around 10% are radio loud.

Seyfert galaxies (Seyfert, 1943) have spiral galaxies as hosts, are radio quiet and classified by their strong emission lines from their centers. Depending on their spectrum they are divided into Seyfert 1 (broad and narrow lines) and Seyfert 2 (only narrow lines) galaxies.

Quasars ('Quasi-stellar Radio Sources') or QSOs ('Quasi-Stellar Objects') display high redshifts and have no optical source that could be associated to them. They are usually radio quiet and possess Seyfert-like spectra, leading to type 1 and type 2 QSOs depending on the emission lines. Radio loud quasars are called *Flat Spectrum Radio Quasars* (FSRQ).

FSRQs, along with *optically violent variable* (OVV) quasars and **BL Lac objects**, belong to the class of **blazars**. They are radio loud, belong to the most luminous sources among AGN and emit light across the entire electromagnetic spectrum. The common feature of blazars is the seeming absence of a host galaxy and existence of a jet emitted from the center. In BL Lac objects thermal emission is generally outshined by the non-thermal emission from jets, leading to an absence of features in the optical and infrared range (see e.g. Chen and Shan, 2011). Their spectral energy distribution (SED) shows a distinct double hump shape with peaks in the synchrotron (Sect. 1.1.2) and γ -ray regime (see e.g. Donato, Ghisellini, et al., 2001). They show strong variability on various timescales across the entire spectrum and jet emission is highly polarized at about $\sim 10\%$ (e.g. Lister and Homan, 2005). They are viewed under a small inclination angle, leading to apparent superluminal motion (Sect. 1.1.4) of jet components (e.g. Kellermann, Lister, Homan, et al., 2004). Their detailed structure and thus intrinsic parameters such as jet speed can only be determined using VLBI observations (Sect. 1.2).

Finally, **Radio Galaxies** are characteristic for their powerful radio jets and are appropriately defined by their radio properties rather than their optical ones. Their hosts are generally elliptical and can be considered as the radio versions of Seyfert galaxies. As such, they are classified as *Broad and Narrow Line Radio Galaxies* (BLRG/NLRG). Additionally they are divided into *Fanaroff-Riley Type I* and *Type II* (Fanaroff and Riley, 1974) based on their morphology, where FR I have a strong nucleus and weaker, broad jets ending in plumes, whereas in FR II, which are in total more luminous, the bright lobes dominate. Compact Symmetric Objects (CSO) display a symmetric double sided structure similar to FR I radio galaxies, but on smaller scales. They are likely younger versions of FR I/II radio galaxies (e.g. Augusto, Gonzalez-Serrano, et al., 2006), where

the jets haven't developed fully yet. This is supported by ages of hot spots determined with kinematic measurements as being less than 10^3 years (e.g. An and Baan, 2012). CSOs are seen edge-on, i.e. under a large inclination angle. For that reason jet components move at low speeds, if motion is detected at all. Their double structure displays an intensity ratio of less than 10 : 1 and steep spectra with a flat spectrum in the central region (e.g. Sokolovsky, Y. Y. Kovalev, et al., 2011). Characteristic to CSOs are their low radio variability of $\lesssim 10\%$ over a timescale of years (Fassnacht and Taylor, 2001) and low radio polarization of $\leq 1\%$ (Peck and Taylor, 2000). Their spectrum peaks at 1 GHz or is steep, classifying CSOs as GHz peaked spectrum sources (GPS) or compact steep spectrum sources (CSS).

Due to the similarities in the observed spectral properties, various models for the **Unification** of all AGN classes were made (Antonucci, 1993; Urry and Padovani, 1995). The unified model of AGN suggests that the different features between the classes originate from the fact that the galaxies are observed under different inclination angles. Figure 1.1 provides a simplified sketch on the structure of active galaxies with different regions such as the broad and narrow line regions. According to this model an AGN consists of a SMBH at the center which is surrounded by a cold torus of dust ($r \sim 1 - 10$ pc) and an inner, hot accretion disk ($r \sim 10^{-3}$ pc) in the same plane. Perpendicular to this plane collimated, jets consisting of relativistically outflowing material are emitted from the nucleus. The broad line region (BLR) is located at a distance of $r \sim 0.01 - 0.1$ pc from the nucleus along the jet and consists of a dense ($n \sim 10^{10} \text{ cm}^{-3}$) and fast rotating medium. Further away at $r \sim 100 - 1000$ pc the narrow line region (NLR) can be found, which is less dense ($n \sim 10^3 - 10^6 \text{ cm}^{-3}$). While the BLR and NLR appear in both radio loud and radio quiet galaxies, jets are only observed in the radio loud case. As the spectral properties only depend on the inclination angle, two types have been defined, where type 1 sources are viewed under a small inclination angle, i.e. a large angle relative to the plane of the dust torus. In the radio loud case this leads to a large increase in a relativistic jet's luminosity due to Doppler boosting effects (see Sect. 1.1.4) which makes the corresponding nucleus and counterjet undetectable. Respectively, if viewed under a large inclination angle, i.e. an edge-on observation, they are defined as type 2 sources (see Fig. 1.1). The various types of AGN are summed up in table 1.1.

Table 1.1: Types of AGN ordered by the unification scheme

	radio quiet	radio loud
Type 1	Seyfert 1	BL Lac
	QSO (Type 1)	FSRQ
Type 2	Seyfert 2	BLRG (FR I + II)
	QSO (Type 2)	NRLG (FR I + II)

Note: Adapted from Müller (2014)

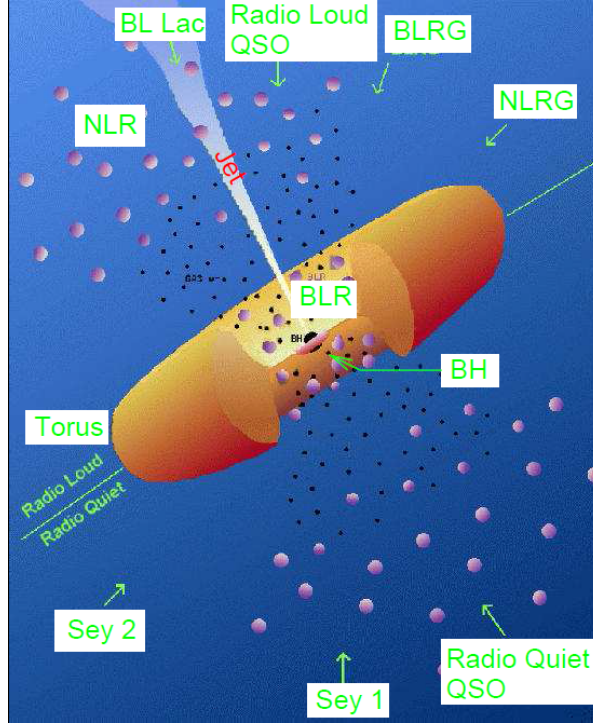


Figure 1.1: Sketch of the unified model of AGN. The model suggests that all observed types of AGN are due to the same type of galaxy observed from different viewing angles. Type 1 galaxies are viewed under a small angle relative to the jet, whereas type 2 sources are seen with a low angle relative to the dust torus. Credit: Urry and Padovani, 1995

1.1.2 Emission processes in jets

Extragalactic jets emit radiation across the entire electromagnetic spectrum and so one major task is determining the dominating processes that lead to these emissions and describing them properly. It is known today that the main physical process causing the low frequency emission is *synchrotron radiation*, also known as *magnetobremstrahlung*, whereas *inverse Compton scattering* dominates the higher frequencies. These two types of emission will be explained briefly here, based on the derivations of Rybicki and Lightman (1979).

Charged particles moving with a velocity \mathbf{v} in a magnetic field \mathbf{B} , specifically electrons here, are accelerated by the Lorentz force $\mathbf{F} = \mathbf{v} \times \mathbf{B}$. This forces the electrons to a helical motion around the magnetic field lines with the frequency $\omega_B = \frac{\omega_L}{\gamma}$ with the Larmor frequency $\omega_L = \frac{eB}{m_e c}$, where e is the elementary charge, and m_e the electron mass, as well as the Lorentz factor $\gamma = \left(\sqrt{1 - \beta^2}\right)^{-1}$ with $\beta = \frac{v}{c}$. Accelerated charged particles emit electromagnetic radiation, which is synchrotron radiation in the case of relativistic electrons with a strongly peaked emission at $\gamma^2 \frac{\omega_L}{2\pi}$. The spectral energy distribution $P_\nu(\gamma)$ of a single particle is given by the product of the emitted power P

and the spectral shape $\phi_\nu(\gamma)$.

$$P_\nu(\gamma) = \frac{1}{6\pi} B^2 \beta^2 \gamma^2 c \sigma_T \phi_\nu(\gamma) \quad (1.1.1)$$

where σ_T is the Thomson cross section. The radiation of a particle travelling at relativistic speeds is beamed forward into a cone with an opening angle $\propto \gamma^{-1}$. An observer looking at the cone detects a short pulse. The emitted spectrum can be computed by weighting the energy distribution with the electron density distribution $n(\gamma)d\gamma$ which follows a power law $n_0\gamma^{-p}d\gamma$ for nonthermal synchrotron radiation. The spectral shape of an electron is well approximated by a peak distribution $\phi_\nu(\gamma) = \delta(\nu - \gamma^2\nu_L)$ at the peak frequency $\gamma^2\nu_L$. The emitted spectrum is then

$$P_\nu = \int_1^\infty P_\nu(\gamma)n(\gamma)d\gamma = \frac{1}{6\pi} c \sigma_T n_0 B^2 \nu_L^{-1} \left(\frac{\nu}{\nu_L} \right)^{-\frac{p-1}{2}} \quad (1.1.2)$$

which is simply a power-law distribution. $\alpha = \frac{1-p}{2}$ is defined as the *spectral index*. Synchrotron radiation itself is strongly polarized and reproduces the non-thermal spectra of blazars very well as opposed to thermal radiation.

The spectrum steepens for the highest-energy electrons as they lose their energy through radiation faster than lower-energy electrons. The optical depth τ_ν is defined as

$$d\tau_\nu = \alpha_\nu ds \quad (1.1.3)$$

with the absorption coefficient α_ν . A medium is optically thick for $\tau_\nu > 1$ and optically thin for $\tau_\nu < 1$. Synchrotron self-absorption is the process of electrons absorbing the very low-energy photons that they emitted. The resulting source function for synchrotron emission is then $S_\nu \propto \nu^{5/2}$, a power law independent of p , i.e. the power-law coefficient of the electron distribution. This process occurs only below a critical frequency (synchrotron self-absorption frequency), where $\tau_\nu = 1$, i.e. the turning point where a medium changes from optically thin to thick. For $\tau_\nu > 1$ it is $S_\nu \propto \nu^{5/2}$ and for $\tau_\nu < 1$, $S_\nu \propto \nu^{-\frac{p-1}{2}}$. Generally larger structures display a turning point at lower frequencies, allowing one to determine the size of a component by observations at different frequencies. The innermost unresolved region of a jet is referred to as the VLBI core, however it does not necessarily coincide with the SMBH at the AGN's center.

The high frequency emission is dominated by Compton scattering which describes the process of inelastic scattering between a photon and a charged particle which leads to an energy-loss for the photon and respectively an energy-gain for the particle. During inverse Compton scattering the process is reversed which means that low-energy photons gain energy instead through up-scattering by relativistic electrons, which lose energy respectively. As for the origin of the photons there are two possibilities: If they originate from the cosmic background radiation, one speaks of External Compton. Otherwise, one refers to Synchrotron Self-Compton if the up-scattered photons are the very same ones

emitted by the electrons within the jet. This energy-loss can in total result in a cooling down of the electron gas, when the photons gain energy, which is referred to as thermal comptonization. This can lead to the so called Compton catastrophe, i.e. a rapid cooling of the electrons yielding a limit for the brightness temperature of $T_b \sim 10^{12}$ K (T_b see Sect. 1.1.3).

1.1.3 Brightness temperature

When modeling relativistic jets, jet components are identified and described as a Gaussian component radiating with a certain *brightness temperature* which is its assumed temperature if the jet component were a black body. The brightness temperature can be calculated according to Y. Y. Kovalev et al. (2005) as

$$T_b = \frac{2 \ln 2}{\pi k_B} \frac{S_{\text{core}} \lambda^2 (1+z)}{\theta_{\text{maj}} \theta_{\text{min}}} . \quad (1.1.4)$$

S_{core} is the flux density of the considered component, λ the emission frequency, k_B the Boltzmann constant, z the redshift and θ_{maj} and θ_{min} the full width at half maximum (FWHM) of an elliptical Gaussian component along the major and minor axis. There are two limits to the maximum brightness temperature, which are the previously mentioned inverse Compton limit of 10^{12} K and the equipartition value of 10^{11} K. However during modelfitting the computed values may often be higher due to various reasons such as Doppler boosting, which need to be taken into consideration.

1.1.4 Relativistic boosting and jet kinematics

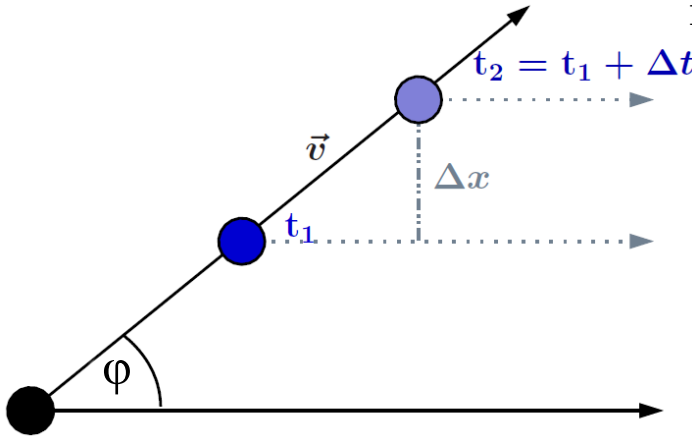


Figure 1.2: Sketched depiction of projection effects causing superluminal motion. A signal is emitted at t_0 and t_1 by an object moving towards an observer with velocity v at an angle ϕ . The relativistic speed causes the object to appear as moving faster than light. (Taken from Müller (2014))

Kinematic analysis of VLBI observations over a time of several years yielded jet speeds higher than the speed of light, which seems unphysical at first, but can be easily explained as a simple projection effect. Consider an object moving at the observer with speed v

at an angle ϕ to the line of sight (LOS) (see Fig. 1.2). A signal is emitted by the object at t_0 as well as $t_1 = t_0 + \Delta t_{\text{emit}}$. Due to c being the maximum speed of information transmission, the observer sees the two signal separated by the time

$$\Delta t_{\text{obs}} = \Delta t_{\text{emit}} \left(1 - \frac{v}{c} \cos(\phi) \right) \quad , \quad (1.1.5)$$

while the observed distance is simply the projection of the travelled distance onto the sky $\Delta l = v \sin(\phi) \Delta t_{\text{emit}}$. Finally, the observed speed is then

$$v_{\text{app}} = \frac{\Delta l}{\Delta t_{\text{obs}}} = \frac{v \sin(\phi)}{1 - \frac{v}{c} \cos(\phi)} \quad (1.1.6)$$

with $\beta_{\text{app}} = \frac{v_{\text{app}}}{c}$. For small ϕ this velocity can very well be greater than c . The relation is plotted in Fig. 1.3 for β_{app} as a function of ϕ for different intrinsic velocities β . The function peaks at very small ϕ , i.e. when the jet points almost directly at the observer, but quickly drops to 0 for $\phi \rightarrow 0$. Additionally, as β increases, the projection effects become stronger, resulting in an overall larger β_{app} , and the maximum of the function moves towards smaller ϕ . From Eq. 1.1.6 follows directly that $\beta_{\text{app}} = \frac{\beta \sin(\phi)}{1 - \beta \cos(\phi)}$ or

$$\beta = \frac{\beta_{\text{app}}}{\beta_{\text{app}} \cos(\phi) + \sin(\phi)} \quad . \quad (1.1.7)$$

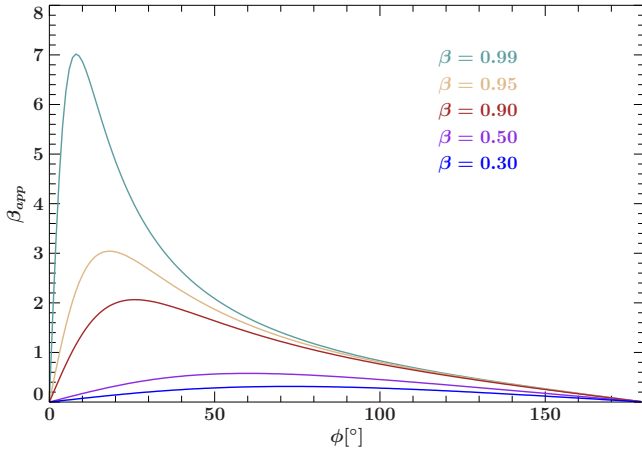


Figure 1.3: Apparent velocity β_{app} plotted as a function of the angle to the line of sight ϕ for different intrinsic velocities β . It is evident that the projection effects increase rapidly with rising β . Additionally, the maximum of the function moves towards smaller angles with increasing β .

Another effect of the jet's relativistic motion is so called Doppler boosting. Due to this effect an incoming jet's flux density is increased and respectively an outgoing jet's flux density is reduced. This is due to the fact that charged particles moving at relativistic speeds do not radiate spherically but rather in a cone with an opening angle of γ^{-1} in their direction of movement. The Doppler factor D is defined as the ratio of observed

and emitted frequency:

$$D = \frac{\nu_{\text{obs}}}{\nu_{\text{emit}}} = \frac{\sqrt{1 - \beta^2}}{1 - \beta \cos(\phi)} = \gamma^{-1} (1 - \beta \cos(\phi))^{-1} \quad . \quad (1.1.8)$$

According to Rybicki and Lightman (1979) the quantity $S_\nu \nu^{-3}$ is invariant under Lorentz transformation. For a jet with a power law spectrum, i.e. $S_\nu \propto \nu^\alpha$, the observed flux density is increased by a factor that is

$$S(\nu_{\text{obs}}) = D^{3-\alpha} S(\nu_{\text{emit}}) \quad . \quad (1.1.9)$$

Doppler boosting explains why in blazars only one jet is visible, while the receding jet, referred to as counterjet, is not visible as its flux density is in fact reduced. With the two previous equations (1.1.8 and 1.1.9) and using the ratio of the flux densities of the jet and counterjet, one gains the equation

$$R = \frac{S_{\text{jet}}}{S_{\text{counter}}} = \left(\frac{1 + \beta \cos(\phi)}{1 - \beta \cos(\phi)} \right)^{i-\alpha} \quad . \quad (1.1.10)$$

For a spherical emission, i.e. if one observes only one "blob", it is $i = 3$. If the jet can be expressed as a series of blobs, one chooses $i = 2$ as the number of spherical emission components scales as the Doppler factor. Using this relation, an upper limit for the angle to the LOS ϕ can be computed.

1.2 Very Long Baseline Interferometry

Finding out how jets are formed and determining the underlying processes is one of the crucial questions of AGN physics and observations. For this purpose high resolutions need to be achieved in order to resolve the innermost regions of AGN, the very regions where jets could possibly be formed. The following explanations closely follow the textbooks by Thompson, Moran, and Swenson (2001) and Burke and Graham-Smith (2010).

The angular resolution θ of a telescope can be computed as

$$\theta \approx 1.22 \frac{\lambda}{D} \quad , \quad (1.2.1)$$

where λ is the wavelength at which the telescope observes and D the telescope's diameter. The intensity distribution of an incoming signal can be described by a Bessel's function, so the factor of 1.22 is simply an approximation of the first Bessel's function vanishing. It is evident that for single-dish observations, i.e. observations utilizing only one telescope, the angular resolution is limited by the technological realization of building large enough telescopes, which is especially problematic for radio observations due to the large observation wavelengths. For instance the largest steerable antenna, namely the Green Bank Telescope in Virginia, USA, which has a diameter of around 101 m (followed by the radio telescope in Effelsberg, Germany with a diameter of 100 m) possesses at an observation wavelength of $\lambda = 3.57$ cm (which roughly corresponds to 8.4 GHz) according to eq. 1.2.1 an angular resolution of $\theta \approx 4.31 \times 10^{-4}$ rad = 88.95 arcsec which is not enough to resolve the distant galactic objects in the sky. For that purpose a technique utilizing interferometry and Fourier transformation was developed known as *Very Long Baseline Interferometry*. In the next sections the theoretical background for VLBI following the textbooks by Thompson et al. (2001) and Burke & Graham-Smith (2010) as well as the basic concepts for analyzing VLBI data with appropriate programs is explained.

1.2.1 Theory of VLBI

The principle of VLBI is to combine several single telescopes to an array in order to simulate one large telescope with sufficient resolution as a consequence. This can be realized by utilizing the properties of an observation under Fourier transformation. With this technique, the resulting telescope possesses a diameter which is equal to the largest distance between two of the array's telescopes. The distance between two of these telescopes is referred to as their *baseline*.

The telescopes may be arranged connected in an array, such as in the Very Large Array (VLA) in New Mexico, or across the globe. The latter can reach baselines of several thousands of kilometers, reaching milliarcsecond resolution, but has an additional need of properly time-correlating the data, whereas in the former case the telescopes are

directly connected, so no synchronization is necessary. However the possible baselines are rather small in comparison, as the VLA for instance only reaches a maximum baseline of 36 km. While the VLA utilizes Fourier transformation, it does not fall under VLBI. One only refers to VLBI for sufficiently long baselines in the range of 10^3 km. The most simple VLBI array consists of only two telescopes and is hence named two-element interferometer. The total power received by one single-dish telescope is limited by its effective area $A_{\text{eff}}(\nu)$

$$P = \int_0^\infty d\nu A_{\text{eff}}(\nu) S(\nu) \quad (1.2.2)$$

where $S(\nu)$ is the source's flux density, i.e. its brightness distribution integrated over the solid angle. An incoming signal reaches the two telescopes at different times separated by the geometrical time delay τ_g . If \mathbf{b} denotes the baseline vector connecting the two antennas and \mathbf{s} is the unit vector pointing at the observed radio source, the geometrical delay can be computed as $\tau_g = \frac{\mathbf{b} \cdot \mathbf{s}}{c}$ (see Fig. 1.4). An instrumental delay τ_i can be added in order to synchronize the signals, however it is necessary to compute the cross-correlation function $R(\tau)$ in order to properly correlate the data. It is defined as the time-averaged product of two amplitudes delayed by τ : $R_{xy}(\tau) = \langle x(t)y(t-\tau) \rangle$. The amplitudes are simply $x(t) = v_1 \cos(2\pi\nu t)$ and $y(t) = v_2 \cos[2\pi(t-\tau_g)]$ as the observed sources are monochromatic. Due to Eq. 1.2.2 the result is proportional to $A_{\text{eff}}(\nu)$:

$$R_{xy}(\tau_g) = A_{\text{eff}}(\mathbf{s}) S \cos(2\pi\nu\tau_g) = A_{\text{eff}}(\mathbf{s}) S \cos(2\pi\mathbf{b}_\lambda \mathbf{s}) \quad (1.2.3)$$

where $\mathbf{b}_\lambda = \frac{\mathbf{b}}{\lambda}$ is the baseline vector in terms of the wavelength.

Suppose that the two-element interferometer is pointing at a source under the direction $\mathbf{s} = \mathbf{s}_0 + \boldsymbol{\sigma}$, where \mathbf{s}_0 denotes the center of the source and is called the phase tracking center. When measuring a source's brightness distribution, the measurement will be affected by the telescope's intrinsic parameters, summarized in its effective area $A_{\text{eff}}(\boldsymbol{\sigma})$. Hence the obtained distribution is the convolution of a telescope's reception (or beam) pattern and the source's brightness distribution $B_\nu(\boldsymbol{\sigma})$.

The interferometer itself measures the Fourier transform of this convolution called the *Visibility* $V_{i,j}$, which is using the fact the convolution product is a simple product in Fourier space

$$V_{i,j} = \int A_{\text{eff}}(\boldsymbol{\sigma}) B_\nu(\boldsymbol{\sigma}) e^{i2\pi\boldsymbol{\sigma} \cdot \mathbf{b}_{i,j}} d\Omega \quad , \quad (1.2.4)$$

i.e. an integration over the solid angle $d\Omega$, where $\mathbf{b}_{i,j}$ denotes multiple baselines with instrumental delay τ_i used to sample the complex visibility function. Using the coordinates (u, v, w) , where w is in direction of \mathbf{s}_0 and u and v form a plane parallel to $\boldsymbol{\sigma}$, the visibility can be described as a function of u and v :

$$V(u, v) = \int_{-\infty}^{\infty} \int_{-\infty}^{\infty} A_{\text{eff}}(x, y) B_\nu(x, y) e^{i2\pi(ux+vy)} dx dy \quad , \quad (1.2.5)$$

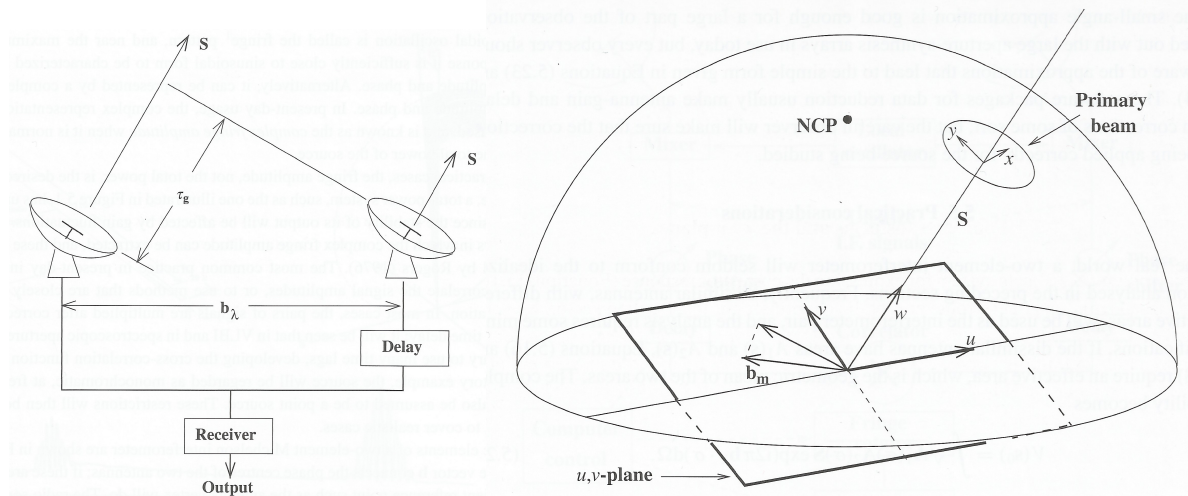


Figure 1.4: Left: Sketch of a two-element interferometer displaying the geometrical time delay τ_g between the two antennas. Right: Illustration of the relationship between the interferometer, a source and the (u, v) -plane. NCP is the north celestial pole. Credit: Burke and Graham-Smith (2010)

A small angle approximation was used, namely that σ is usually very small, in order to use the spatial coordinates x and y for integration, with u then being parallel to x . The coordinates $u = \nu \cdot b \cos(\zeta)/c$ and $v = \nu \cdot b \sin(\zeta)/c$ are the spatial frequencies, with the zenith angle ζ , the baseline length b and the observation frequency ν . The plane spanned by these coordinates is appropriately named (u, v) -plane. This means that the process of measurement is covering the (u, v) -plane in Fourier space, where the coverage is equal to the amount of information gained from the source's brightness distribution. One integration period corresponds to one point in the (u, v) -plane, hence the limitation of radio interferometry is the inability to cover the entire, infinite (u, v) -plane by measurements.

Figure 1.5 shows the (u, v) -coverage of fake data, used as an example here. Each full or partially filled ellipse belongs to one two-element interferometer, where the length of the ellipse's major axis is equal to the interferometer's baseline length. In radio interferometry the Earth's rotation is utilized in order to sample more points in the (u, v) -plane, as the projected baselines change with the rotation. The sampling reaches the starting point after a measuring time of 12 hours, where the deviation from a circle is given by the interferometer's declination, with $\pm 90^\circ$ (i.e. the poles) corresponding to a circle and 0° to a line. This method is named *Earth rotation synthesis*. In order to fill most of the (u, v) -plane, telescopes across the globe are correlated for measurement, where longer baselines reach high resolutions, while shorter ones provide high sensitivities for larger scale structures.

The sampled (u, v) -coverage then needs to be inversely transformed and deconvolved

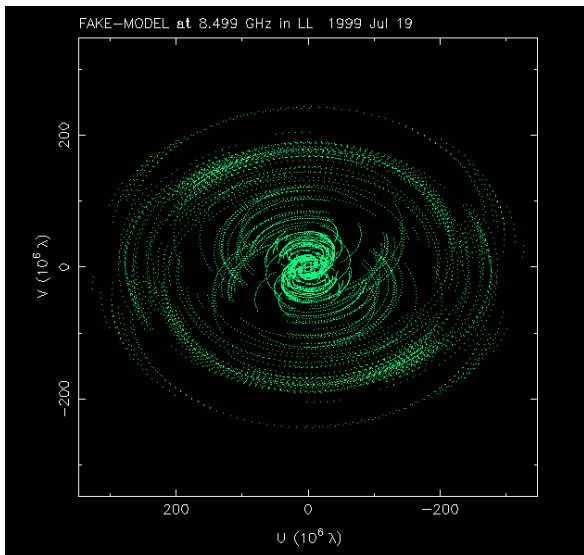


Figure 1.5: Plot displaying an exemplary (u, v) -coverage at 8.4 GHz. Each (partially filled) ellipse corresponds to one baseline, where the major axis is equal to the baseline length.

in order to gain the intrinsic brightness distribution. The gaps within the coverage correlate to errors and artifacts in the brightness distribution as a perfect recovery is only possible by covering the entire (u, v) -plane. The amount of sampling, i.e. the (u, v) -coverage, can be described by the sampling function $W(u, v)$. An additional weighting factor $w(u, v)$ is added, to describe the measured visibility:

$$V_{\text{measured}}(u, v) = W(u, v)w(u, v)V(u, v) \quad . \quad (1.2.6)$$

The factor $w(u, v)$ allows one to better address different kinds of sources, such as compact or more extended sources. For instance, natural weighting, which gives a higher weight to well sampled regions of the (u, v) -plane, reaches high point-source sensitivity, but lowers the resolution as a result, whereas uniform weighting, where parts of the (u, v) -plane are weighted inversely proportional to their number of visibilities, provides higher resolution, but also a higher noise level.

1.2.2 Analyzing VLBI data

Several steps need to be taken when analyzing VLBI data, starting with an a priori amplitude and phase calibration via AIPS (Astronomical Image Processing System, Greisen, 2003), where the amount of data is heavily reduced. More information on the procedure involving AIPS can be found in Cotton (1995) and Diamond (1995).

As mentioned before, in order to reconstruct the initial image, one must first apply the inverse Fourier transformation to the visibility function and then deconvolve the beam pattern and the brightness distribution. Due to the gaps in the (u, v) -coverage, the brightness distribution needs to be interpolated using the available data points. A powerful tool for this purpose is the program DIFMAP (Shepherd, 1997), which provides

a numerical solution utilizing the `clean` algorithm (Högbom, 1974).

The `clean` command in DIFMAP models the source’s brightness distribution by setting δ -components, i.e. point sources, within an area set by the user (“windows”) and subtracting the flux density given by the model from the flux density given by the data. This process is combined with self-calibration in amplitude and phase. During self-calibration, the data points themselves are changed and adjusted to better agree with the model. For the self-calibration method to be possible, the source must have been observable by at least 4 telescopes at all times (or 3 for only phase calibration, see e.g. Felli and Spencer, 1989) After one `clean` step, one uses only phase self-calibration, whereas after cleaning (and phase self-calibrating) sufficiently often, amplitude self-calibration is done for a specific time interval. This process is repeated with subsequently shorter time increments for amplitude self-calibration until the clean image with the best model is retrieved, with the clean beam being approximated by a Gaussian.

With the `modelfit` command, elliptical Gaussian components can be used to describe the source’s structure with a more simple model than the one in the clean image. One such component is defined by its major and minor axis, the position angle (which is arbitrary for a circular component), the integrated flux and its position. As the obtained model is a lot simpler, it is better suited for studying the source’s structure and its development over time, e.g. a kinematic analysis. The underlying algorithm is based on Levenberg (1944).

As DIFMAP does not give any uncertainties for its calculations, the *Interactive Spectral Interpretation System* (ISIS Houck and Denicola, 2000) is used for further calculations using the FITS files (Flexible Image Transport System) given by DIFMAP to compute errors and perform χ^2 analyses, such as linear regression.

1.2.3 TANAMI

Tracking Active Galactic Nuclei with Austral Milliarcsecond Interferometry, or TANAMI, is the only multiwavelength monitoring program which includes VLBI observations set to observe and monitor parsec-scale structures of extragalactic γ -ray sources south of -30° . The information of this section is based on the papers by Kadler, Ojha, and TANAMI Collaboration (2015) and Ojha, Kadler, et al. (2010).

The goal of TANAMI is to investigate the connection between the parsec-scale jet properties and their γ -ray emission, first suggested by observations of the EGRET detector (Compton Gamma Ray Observatory, Thompson et al. 1993) and later confirmed (e.g. Ackermann et al., 2015). TANAMI VLBI observations operate at two frequencies, namely 8.4 GHz and 22.3 GHz. The VLBI data is then combined with associated multiwavelength observations in order to study the broadband spectrum and its behaviour over time. The VLBI observations contribute by providing information on parsec-scale properties such as the apparent jet speed, inclination and opening angles as well as the overall structure. Some of the key aspects that need to be examined by TANAMI are if and how the parsec-scale structures and their changes influence high-energy flaring,

where and how the high energy photons of X-rays and γ -rays are produced as well as what jets are made of and what their detailed structure is.

The TANAMI array includes all telescopes of the Australian Long Baseline Array (LBA). Additionally observations are made with telescopes at NASA's Deep Space Network (DSN) at Tidbinbilla, the South-African Hartebeeshoek 26 m antenna, the 9 m German Antarctic Receiving Station (GARS) in O'Higgins, Antarctica since 2009 as well as the 6 m Transportable Integrated Geodetic Observatory (TIGO) in Chile. Since 2011 the Warkworth, Katherine and Yarragadee antennas are also part of TANAMI observations as well as the ASKAP Radio Telescope of the Australian Telescope National Facility in Murchinson, western Australia. All telescopes are listed in Table 1.2. With these telescopes, typically angular resolutions in the range of a few mas are reached, sometimes even below 1 mas.

Table 1.2: Telescopes belonging to the TANAMI array
(Adapted from Müller (2014))

Telescope	Diameter (meters)	Location
Parkes	64	Parkes, New South Wales, Australia
ATCA	5×22	Narrabri, New South Wales, Australia
Mopra	22	Coonabarabran, New South Wales, Australia
Hobart	26	Mt. Pleasant, Tasmania, Australia
Ceduna	30	Ceduna, South Australia, Australia
Hartebeesthoek ^a	26	Hartebeesthoek, South Africa
DSS43 ^b	70	Tidbinbilla, ACT, Australia
DSS45 ^b	34	Tidbinbilla, ACT, Australia
O'Higgins ^c	9	O'Higgins, Antarctica
TIGO ^c	6	Concepcion, Chile
Warkworth	12	Auckland, New Zealand
Katherine	12	Northern Territory, Australia
Yarragadee	12	Western Australia
ASKAP	36×12	Murchinson, Western Australia

Note: ^(a) Unavailable between Sept. 2008 and Sept. 2010 due to a major failure.

^(b) Operated by the Deep Space Network of the National Aeronautics and Space Administration.

^(c) Operated by the Bundesamt für Kartographie und Geodäsie (BKG)

1.3 Previous results

PMN J1603–4904, also known as PKS 1600–489, is a rather unusual radio-loud object located close to the galactic plane ($l = 332.15^\circ$, $b = 2.57^\circ$) and on the southern sky (RA = 16 h 3 min 50.7 s, DEC = -49° 4 min 5 s¹). It first gained a lot of attention when it was detected in the γ -rays and is one of the brightest γ -ray sources detected by *Fermi*/LAT (Abdo, Ackermann, Ajello, et al., 2010, Nolan, Abdo, et al., 2012). The association with the γ -ray source 1FGLJ1603.8–4903 lead to its inclusion in the TANAMI sample (Müller, 2014). Due to its absence of optical emission lines, although strongly suffering from extinction, and broadband properties it has been first classified as a low synchrotron peaked (LSP) BL Lac object with a very hard γ -spectrum, high brightness and low variability. However TANAMI measurements are not consistent with this classification as they revealed an atypical mas-scale structure for a BL Lac object. Based on the results of Müller, Kadler, et al. (2014) as well as the PhD thesis by Müller (2014) a classification as a *Compact Symmetric Object* (CSO), which are assumed to be young radio galaxies in their earliest stages of development, seems more reasonable. There has been one known redshift $z = 0.18 \pm 0.01$ for PMN J1603–4904 (Müller et al., 2015) through X-ray observations, however new optical-NIR spectroscopy (Goldoni, Pita, et al., 2015) revealed emission lines which resulted in a redshift $z = 0.2321 \pm 0.0004$ that is different to the one previously determined. In the following sections I will list in more detail the currently known results about PMN J1603–4904 based on the aforementioned papers by Müller et al. and Goldoni et al. as well as Müller (2014). For this work I have imaged two new epochs of VLBI data on PMN J1603–4904, fitted models based on a simple three component approach as well as a more complex approach and made a kinematic analysis for the simple model to test the previous assumptions on their consistency and determine an upper limit for the jet speed.

1.3.1 Measured redshifts

Two different papers computed a redshift for PMN J1603–4904 by using emission lines in two different spectra and received different values. The first measurement was done in the 2–10 keV X-ray band (Müller et al., 2015) through quasi-simultaneous observations with *XMM-Newton* (Jansen, Lumb, et al., 2001) and *Suzaku* (Koyama, Tsunemi, et al., 2007) in 2013 September. Previous optical measurements constrained the redshift to $z \lesssim 4.24$ and previous *Swift*/XRT observations were not accurate enough. The simultaneous data was fitted with an absorbed power-law component and a Gaussian emission line. Cross-calibration constants were used as well to account for relative flux calibrations of the instruments. The resulting spectrum is shown in Fig. 1.6. An emission line is clearly visible and can be modeled by a Gaussian component at (5.44 ± 0.05) keV with an equivalent width of $EW = (200 \pm 90)$ eV. The Fe K α transition produces the most

¹<http://ned.ipac.caltech.edu/>

prominent line feature in the observed range, hence this line was considered to be the most probable line emitted by PMN J1603–4904. This yields a redshift of $z = 0.18 \pm 0.01$ and a luminosity distance of (872 ± 54) Mpc.

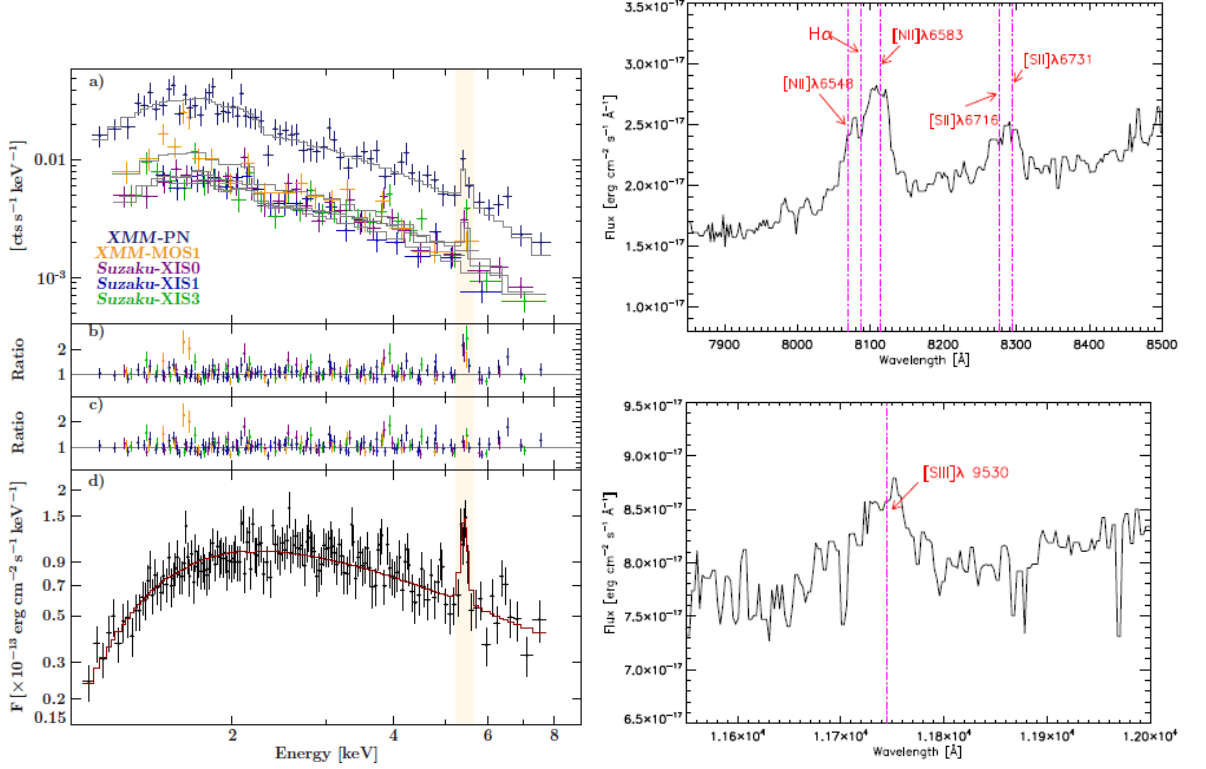


Figure 1.6: Left: Combined fit of the quasi-simultaneous data from measurements with *XMM-Newton* and *Suzaku*. (a) displays the count spectrum with an absorbed power law and a Gaussian emission line (gray) at $\sim 5.44 \pm 0.05$ keV, (b) shows the ratio of data to model for an absorbed power law and (c) including a Gaussian emission line. (d) shows the combined spectrum of all data sets with the best-fit model (red). Credit: Müller et al. (2015)

Right: Sections of the X-shooter spectrum displaying the detected features. The upper panel shows the H α -[NIII] complex and [SII] λ 6716, 6731 and the lower panel the [SIII] λ 9530 feature. Credit: Goldoni, Pita, et al. (2015)

Another observation was done later with the UV-NIR VLT/X-shooter spectrograph (Vernet, Dekker, et al., 2011) by Goldoni, Pita, et al. (2015) which started operations in October 2009 on the VLT. Two observations were performed on 2015 April 30 and 2015 May 13. The detected spectrum is mostly smooth, likely non thermal and does not show lines typical for an elliptical galaxy, i.e. narrow lines or strong absorption lines. No emission lines were found that were consistent with the redshift determined by Müller et al. (2015). However features were found at $\sim 8100, 8250$ and 11700 Å (see Fig.

1.6) that can be interpreted as the $H\alpha$ -[NII] complex, the doublet [SII] $\lambda\lambda$ 6716,6731 as well as [SIII] λ 9530. A single Gaussian fit to the 11700 Å feature yields a redshift of $z = 0.2321 \pm 0.0004$ which would result in an emission line at 6.7 keV for the one detected in Müller et al. (2015). These results favor the scenario of PMN J1603–4904 being of the CSO type rather than a BL Lac object, however a misaligned FSRQ is suggested as well.

1.3.2 Multiwavelength properties

PMN J1603–4904 has been observed as part of the extended TANAMI sample for seven times between 2009 February and 2013 March. The results of the first five epochs as well as other multiwavelength properties, which can be found in Müller, Kadler, et al. (2014) (first three epochs) and Müller (2014), are presented in this section. The TANAMI sample is monitored regularly with the Australian Telescope Array (ATCA), where so called snapshot observations are made at frequencies of 5.5, 9, 17, 19, 38 and 40 GHz with a band of 2 GHz for each frequency. The flux densities are calibrated against the primary flux calibrator PKS 1934–638 and Uranus at 7 mm and the primary beam widths range from 10' at 5.5 GHz to 1' at 40 GHz (Stevens, Edwards, Ojha, et al., 2012). Regardless of the exact ATCA configuration, PMN J1603–4904 is unresolved in all snapshot measurements.

Each VLBI observation was taken at 8.4 GHz with an additional observation in 2010 May at 22.3 GHz. As each measurement used a different array configuration, the (u, v) -coverage, sensitivity and angular resolution differ between the epochs resulting in differing image qualities, which is especially apparent for the 2011 observation. Figure 1.7 show the first five PMN J1603–4904 epochs at 8.4 GHz. Additional data on the observations and image parameters are listed in Table 2.1. These results and first modelfitting data are from Müller, 2014.

PMN J1603–4904 displays a very compact structure with a western to eastern extension of about -8 to 6 mas and is very symmetric in its properties. According to Ojha, Kadler, et al. (2010) $\sim 15 - 20\%$ need to be applied to the flux values as an estimate of the absolute calibration uncertainties. Within these error margins, there is no variability in the flux density for the first five epochs, with values ranging from 570 mJy to 630 mJy. These varying values are also due to changes in the array configuration between epochs. This lack of variability is also supported by the radio light curve from the ATCA snapshot monitoring shown in Fig. 1.8 (Müller, Kadler, et al., 2014), where no variability can be detected between 2009 and 2012. However low-level variability on longer timescales is detectable.

The structure was fitted with a simple three-component model, where an elliptical Gaussian (circular for the 2010 December epoch) is set in the most compact and most luminous region in the middle and two circular Gaussians are applied to the eastern and western regions (see Fig. 2.6). The specific parameters are listed in Table 2.2. Again within the uncertainties no variability in flux can be determined and the brightness

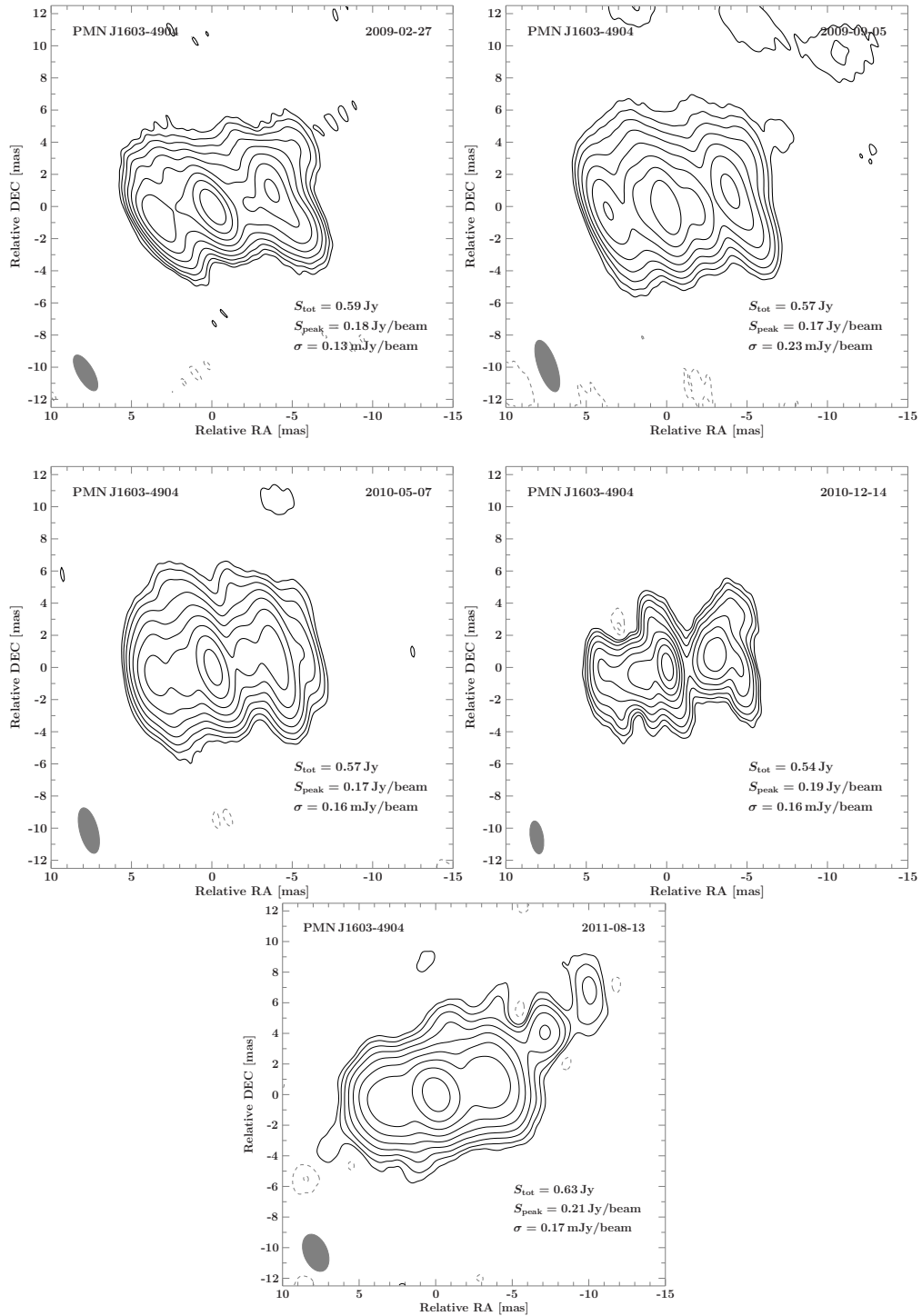


Figure 1.7: Clean images of the first five 8.4 GHz TANAMI epochs of PMN J1603–4904 are shown. The parameters listed within are the total integrated flux S_{tot} , the highest flux per beam S_{peak} and the noise σ . The contours scale logarithmically with a factor of 2, where the lowest level is set to the 3σ -noise level. The size of the restoring beam is shown in the lower left corner of each image as a grey ellipse. The images have been previously published and analyzed in Müller, Kadler, et al., 2014 and Müller, 2014.

temperature is rather constant for the two circular components at $\sim (4 - 6) \times 10^8$ K (first 5 data sets in Fig. 2.3 and Fig. 2.4). The central component has a brightness temperature of $\gtrsim 10^{10}$ K and shows an increase for the 2010 December epoch followed by a drop to roughly the past values. This can be attributed to different resolution, as the array configuration in the 2010 December epoch is able to resolve the compact region in the middle. Hence the region is modelled by a circular Gaussian of smaller area than an elliptical one, which leads to the observed increase in T_b . For these epochs the eastern component's flux density is about (0.2 ± 0.1) Jy smaller and it is about 0.6 mas closer to the center than the western component (see Müller, 2014 and Müller, Kadler, et al., 2014).

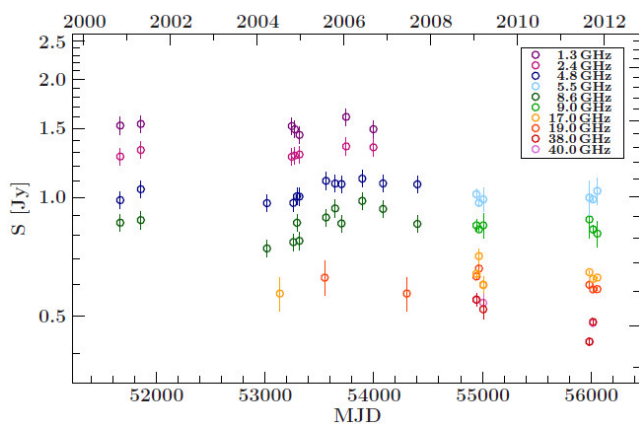


Figure 1.8: Radio light curve of PMN J1603–4904 from the ATCA snapshot monitoring at 6 frequencies. No variability has been detected between 2009 and 2012, however small long-term variability is visible. Credit: Müller, Kadler, et al. (2014)

By setting the component positions relative to the central one, which is assumed to be the core due to its compact nature, an estimate of the spatial variability, i.e. the component speed, can be determined. The data points as well as the evolution determined by linear regression containing the first five epochs are shown in Fig. 1.9. No proper motion could be detected for the components, i.e. they are stationary within their errors. An upper limit for the speed was determined by Müller (2014) to be $|v_{\text{app}}| < 0.2$ mas/yr.

The 22.3 GHz observation suffered from a sparse (u, v) -coverage containing only shorter baselines. As a result the data could not be modeled with the `clean` algorithm used for all 8.4 GHz epochs. Instead, in Müller, Kadler, et al. (2014) the simple three-component approach was applied to the 22.3 GHz data in order to be able to analyze the structural properties at this frequency and combine it with the 8.4 GHz results to compute the spectral index. Due to the steep spectra of jets it is unlikely in VLBI that the 22.3 GHz data would show more extended emission than the 8.4 GHz data. Thus it is unlikely that the emission region at 22.3 GHz is larger than at 8.4 GHz. This model at 22.3 GHz is hence referred to as the 'extended' model. For the spectral index profiles, absolute calibration uncertainties could formally be assigned in both frequency bands, however they would neglect the structural uncertainties at 22.3 GHz due to sparse (u, v) -coverage. Another 'compact' model consisting of only one elliptical Gaussian was fitted to constrain the

uncertainties. The extended model gives a spectral index profile of $-2.0 \lesssim \alpha \lesssim -1.0$ for the eastern and western wings and $-0.75 \lesssim \alpha \lesssim -0.25$ in the center. The compact model displays the same spectrum in the center, but reaches unphysical values of $\alpha \ll -2.0$ in the eastern and western regions. Additionally the compact model allows different alignments with the 8.4 GHz image, i.e. the single component could also be associated with the eastern component at 8.4 GHz. Hence the compact model does not lead to a self-consistent dual-frequency model. For these reasons the central feature is the most likely candidate for the core of PMN J1603–4904.

The possible classification scenarios based on these results will be discussed in context with the new epochs in Sect. 3.2.

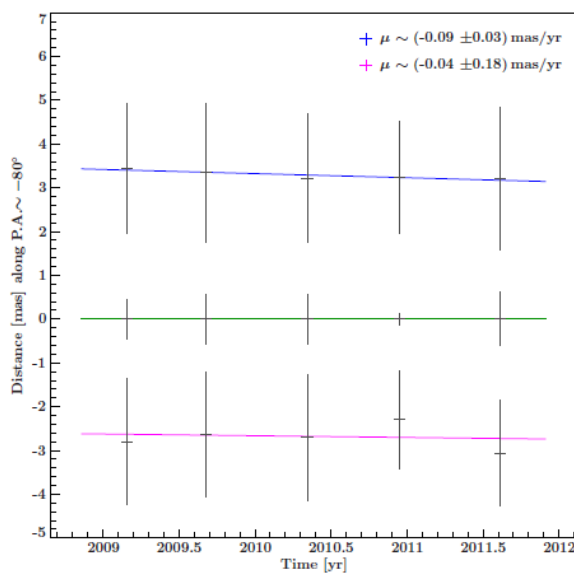


Figure 1.9: Position evolution of the eastern (pink) and western (blue) model components relative to the central (green) one for the first five PMN J1603–4904 epochs. The errors are estimated by the size of the semi-major axis of the Gaussian component. Linear regression yields speeds of $\mu \sim (-0.09 \pm 0.03)$ mas/yr and $\mu \sim (-0.04 \pm 0.18)$ mas/yr, meaning that all components are stationary within errors. Credit: Müller (2014)

2 TANAMI VLBI Observations of PMN J1603–4904 in 2012 and 2013

2.1 Imaging and modelfitting

Two new VLBI observations of PMN J1603–4904 were conducted in 2012 September and 2013 March. Recovering and model fitting the clean images as well as analyzing the kinematic behaviour with inclusion of these new epochs is the main part of this thesis. This section will focus on describing the cleaned images and how they fit with the past epochs as well as discussing possible models.

Both epochs lack some data on the shortest baselines due to the absence of Mopra in the array configuration. Figure 2.1 displays the (u, v) -coverage of both of the new epochs, where the lack of short baselines is evident. The images were recovered using the `clean` algorithm within `DIFMAP` and can be seen in Fig. 2.2. Additional information and image parameters on these two and the remaining epochs are listed in Table 2.1. The recovering beams are quite smaller in size, which can however be attributed to different array configurations as well as imaging procedures in `DIFMAP`, e.g. the detailed placement of windows.

There is an increase in flux density in the 2013 epoch with a total integrated flux of 730 mJy, however within the conservative estimates for uncertainties of $\sim 15 - 20\%$ (Ojha, Kadler, et al., 2010) the flux density is constant within the errors and within all epochs, i.e. there are no signs of variability. The overall structure of PMN J1603–4904 remains the same over the extent of all epochs, with a compact, bright region in the center and two more extended regions to the East and West with a constant western to eastern extension of about -7 to 6 mas. It should be noted that the 2012 epoch image is very consistent with the images prior to 2011 August, where the western region expands more to the North-West and South-West on the edge. This can be seen best for the 2010 December epoch, where PMN J1603–4904 was resolved best. The 2013 epoch reveals a wilder structure, most notably an excess region at the approximate relative coordinates $RA= 1$ mas, $DEC= 5$ mas, which did not appear to such an extent in the other epochs. It is likely that this structure belongs to the source as an exclusion would deteriorate the image quality and reduce the cleaning depth, resulting in a higher noise level. If no windows are set there, some flux remains at where the region is located.

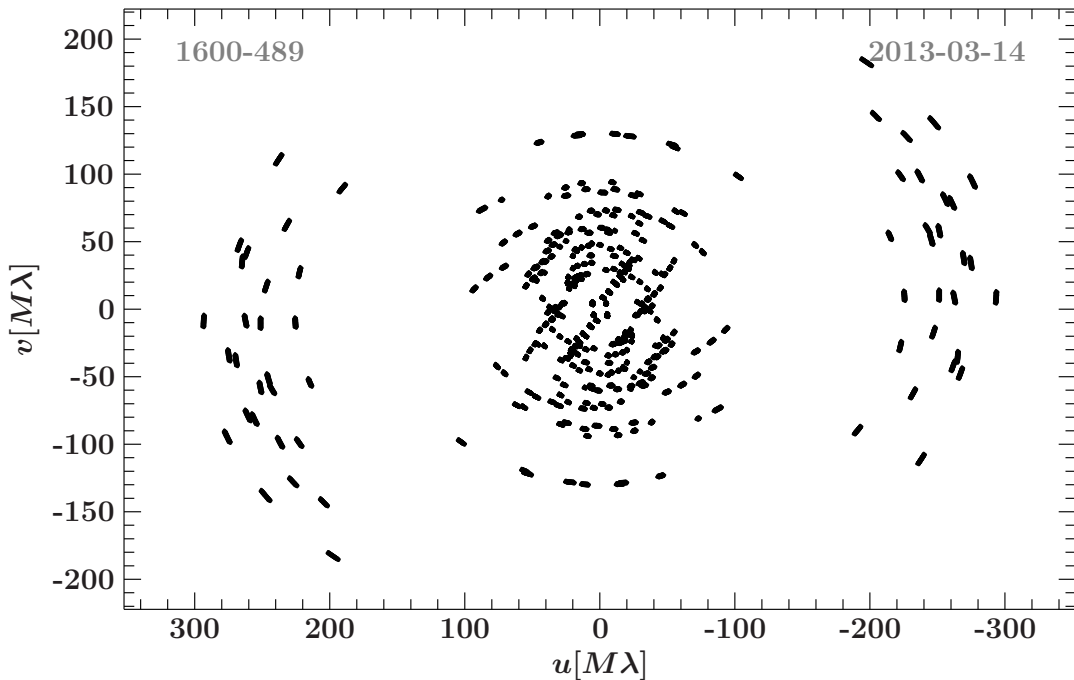


Figure 2.1: (u, v) -coverage of the new 2013 March PMN J1603–4904 epoch. This epoch was chosen as it contains the largest amount of telescopes among all observations and thus has the most complete (u, v) -coverage. Due to the absence of Mopra in both arrays, there is a lack of short baselines.

Additionally there are two small regions of excess flux to the west of PMN J1603–4904 which became visible in the 2011 August epoch, most likely due to the increased sensitivity as long baselines were very sparse for this observation. These regions reappear at roughly the same position and similar shape in 2012 and again in 2013, albeit in a more deviated form and position. It is unclear whether or not these excess regions belong to PMN J1603–4904 or not, however the image quality increases if they are taken into account and they remain in the end even if no windows are set at their positions.

For a first approach the three-component model was adopted from Müller, Kadler, et al. (2014) and applied to the new data. Both epochs were fitted by setting an elliptical Gaussian component in the center and adding two circular Gaussians to model the eastern and western wings. The resulting models are shown in Fig. 2.6 with detailed parameters listed in Table 2.2. On average the western component is brighter than the eastern component by (0.034 ± 0.008) Jy and around (0.57 ± 0.09) mas farther away from the center. These values have been computed as an average over all epochs.

The next section will present the results of a kinematic analysis by describing the time evolution of the components' parameters.

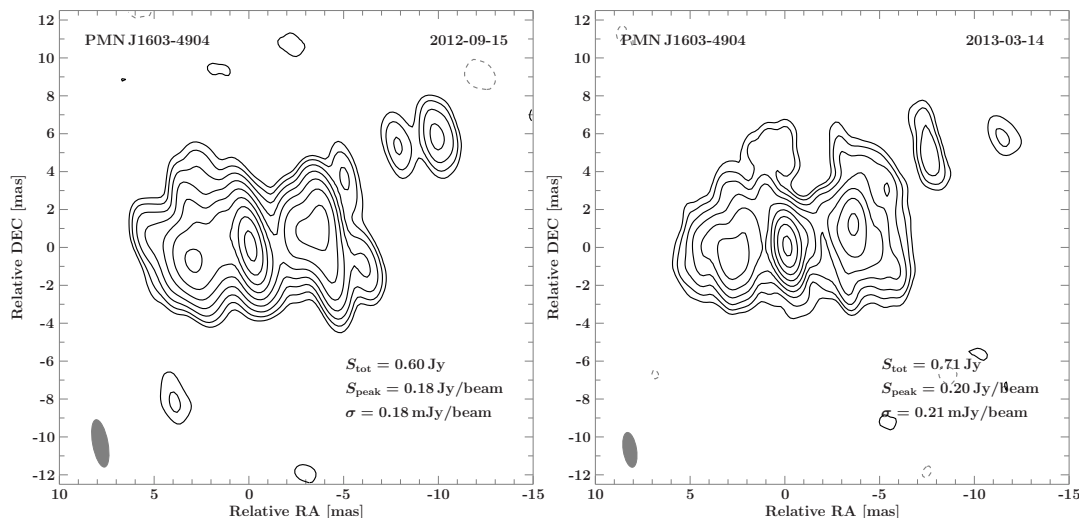


Figure 2.2: Clean images of the two most recent epochs of PMN J1603–4904. The contours, quantities and beam pattern are the same as in Fig. 1.7. The overall structure did not change significantly compared to the past observation and can be attributed to different array configurations.

Table 2.1: TANAMI VLBI observations of PMN J1603–4904 at 8.4 and 22.3 GHz and image parameters

Date yyyy-mm-dd	Frequency [GHz]	Array Configuration ^a	S_{tot} [Jy]	S_{peak} [Jy/beam]	σ [mJy/beam]	b_{maj}^c [mas]	b_{min}^c [mas]	P.A. ^c [°]
2009-02-23/27 ^b	8.4	PKS-CD-HO-MP-AT-DSS43-DSS34-TC-OH	0.59	0.18	0.13	2.51	0.98	30.1
2009-09-06	8.4	PKS-CD-HO-MP-DSS43-TC	0.57	0.17	0.23	3.36	1.15	19.2
2010-05-07	8.4	PKS-CD-HO-MP-AT-TC	0.57	0.17	0.16	2.91	1.12	14.9
2010-12-14	8.4	MP-HO-DSS43-DSS34-CD-AT	0.54	0.19	0.16	2.06	0.80	0.04
2011-08-14	8.4	YG-DSS43-TC-PKS-MP-KE-HO-CD-AT	0.63	0.21	0.17	2.54	1.55	22.6
2012-09-15	8.4	AK-AT-CD-HH-HO-KE-PKS-TC	0.60	0.18	0.18	2.53	0.81	10.4
2013-03-14	8.4	AK-AT-CD-HO-KE-PA-TC-WW-DSS34 ^d -DSS43 ^d	0.71	0.20	0.21	1.85	0.70	9.0
2010-05-05	22.3	PKS-HO-MP-AT	0.29	0.14	0.35	2.09	1.16	83.9

Note: ^(a) AT: Australia Telescope Compact Array, CD: Ceduna, HO: Hobart, MP: Mopra, OH: GARS/O’Higgins, PKS: Parkes, TC: TIGO, DSS34 & 43: Tidbinbilla (34 m & 70 m), YG: Yarragadee, KE: Katherine, HH: Hartebeesthoek, AK: ASKAP ^(b) Due to poor (u, v) -coverage compared to the rest of the observations at 8.4 GHz, the two February measurements were combined. ^(c) b_{maj} and b_{min} are the major and minor axis of the restoring beam and P.A. its position angle. ^(d) The 2013 epoch contained two subarrays, where DSS34 and DSS43 only appeared in one of the subarrays. (Table entries from pre-2012 epochs taken from Müller, 2014)

Table 2.2: Model fit parameters for the three component model at 8.4 GHz

S^a [Jy]	d^b [mas]	θ^b [°]	a_{maj}^c [mas]	a_{min}^c [mas]	P.A. ^c [°]	T_b^d [10 ⁹ K]	$(1+z_1)T_b^e$ [10 ⁹ K]	$(1+z_2)T_b^e$ [10 ⁹ K]
2009-02-23/27								
0.17	2.8	97.0	2.9	2.9	138.0	0.35	0.41	0.44
0.22	0.0	—	0.9	0.5	33.0	9.1	10.7	11.20
0.20	3.4	−79.0	3.0	3.0	−114.0	0.39	0.46	0.48
2009-09-05								
0.16	2.6	90.0	2.9	2.9	−155.0	0.34	0.40	0.42
0.22	0.0	—	1.1	0.4	17.0	8.6	10.10	10.81
0.19	3.3	−77.0	3.2	3.2	−153.0	0.32	0.38	0.41
2010-05-07								
0.17	2.7	98.0	3.0	3.0	177.0	0.35	0.41	0.44
0.21	0.0	—	1.1	0.4	12.0	8.6	10.10	10.71
0.19	3.2	−78.0	2.9	2.9	20.0	0.38	0.45	0.48
2010-12-14								
0.16	2.3	105.8	2.3	2.3	61.7	0.54	0.63	0.68
0.22	0.0	—	0.3	0.3	45.64	56.1	65.9	69.79
0.17	3.2	−78.5	2.6	2.6	−39.1	0.45	0.53	0.55
2011-08-14								
0.15	3.1	100.2	2.4	2.4	−8.9	0.44	0.52	0.57
0.27	0.0	—	1.2	0.9	−33.1	4.19	4.92	5.26
0.21	3.2	−75.4	3.3	3.3	−58.2	0.34	0.40	0.42
2012-09-15								
0.17	2.8	95.8	2.6	2.6	5.5	0.44	0.52	0.55
0.23	0.0	—	0.86	0.42	7.2	10.97	12.94	13.51
0.20	3.4	−78.0	2.7	2.7	8.6	0.47	0.56	0.58
2013-03-14								
0.18	2.8	94.2	2.7	2.7	8.4	0.44	0.52	0.54
0.27	0.0	—	0.84	0.44	3.4	12.73	15.02	15.68
0.25	3.4	−76.0	3.10	3.10	0.0	0.46	0.54	0.56

- Note:** (a) Integrated flux density of the model component
(b) Distance and position angle of the component from the phase center
(c) Major and minor axes of the component and position angle of the major axis
(d) Brightness temperature of the component at $z = 0$
(e) Corrected brightness temperature with $z_1 = 0.18$ and $z_2 = 0.2321$.
(Table entries from pre-2012 epochs taken from Müller, 2014)

2.2 Kinematic analysis

In order to analyze the movement of the components and their overall time evolution, their position needs to be studied relative to one of the components, whose position is set as constant. Due to its compact nature, high flux density and flat spectrum (Müller, Kadler, et al., 2014) the central component is the most likely candidate for the jet core. For comparison the speed was measured relative to each of the components.

Figure 2.6 gives an overview of the three-component model and their time evolution. The Gaussian components are placed where the flux density reaches peak values in the clean image. The central component, which is referred to as "Core" due to the reason given above is very small in its extension throughout all epochs and was always fitted by an elliptical Gaussian except in the 2010 December observation. In Müller (2014) this is attributed to an increased resolution, making it possible to better resolve smaller structures in the core region. "W1" and "E1" refer to the western and eastern components respectively. They are consistently modelled as two circular Gaussians.

The flux density for each component remains constant within the conventional uncertainties of 15 – 20 % (Ojha, Kadler, et al., 2010). The development over time is plotted in Fig. 2.3. However the last epoch seems to indicate an increase in flux for all components as already suggested by the total integrated flux listed in Table 2.1. This however

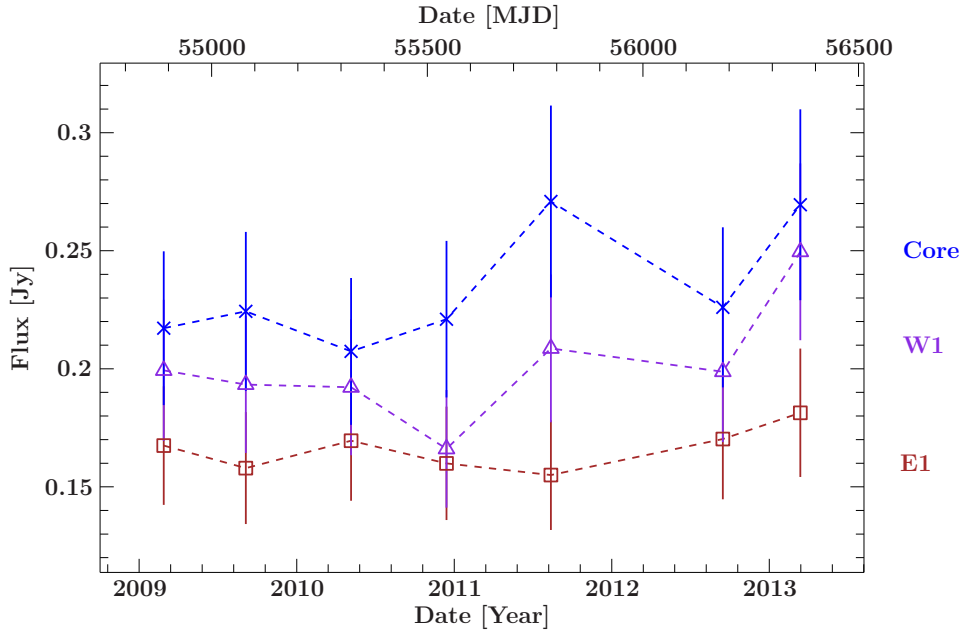


Figure 2.3: Plotted are the flux densities of each component over the time. E1, Core, W1 are the eastern, central and western components. The error bars are set to 15 % of the flux density value. Within the conventional uncertainties of 15 – 20 % all values coincide for each respective component.

cannot be confirmed within the errors nor does PMN J1603–4904 show any variability

between 2009 and 2012 as measured by the ATCA monitoring shown in Fig. 1.8. The 2011 August epoch also displays a larger flux density, however mainly for the core. As there was very sparse (u, v) -coverage on the longest baselines, this epoch’s sensitivity is higher, but pays by having a lower resolution. This could very well be the reason for the measured increase in flux in this epoch, but cannot be applied to the 2013 epoch.

The brightness temperature of the eastern and western components (Fig. 2.4, left) remains at a constant level of $T_b \sim (4 - 6) \times 10^8$ K, which can be seen directly by looking at the major axis (Fig. 2.4, right) and flux density (Fig. 2.3). While the size of W1 shows similarly scattered values across all epochs, E1 displays a drop in size in 2010 Dec. and growing consistently back to its previous size. The dispersion of these values however is not large enough to cause a notable change in brightness temperature as the flux density remains consistent as well. On the other hand the core displays a peak brightness temperature in 2010 Dec., reaching almost 10^{11} K, which is due to the core being modeled as a circular rather than an elliptical Gaussian, leading to a small major axis. Respectively the low resolution of the 2011 observation resulted in a larger than usual major axis, leading to a smaller than usual brightness temperature regardless of higher flux. The core’s T_b is constant at $\sim 10^{10}$ K for the remaining five epochs.

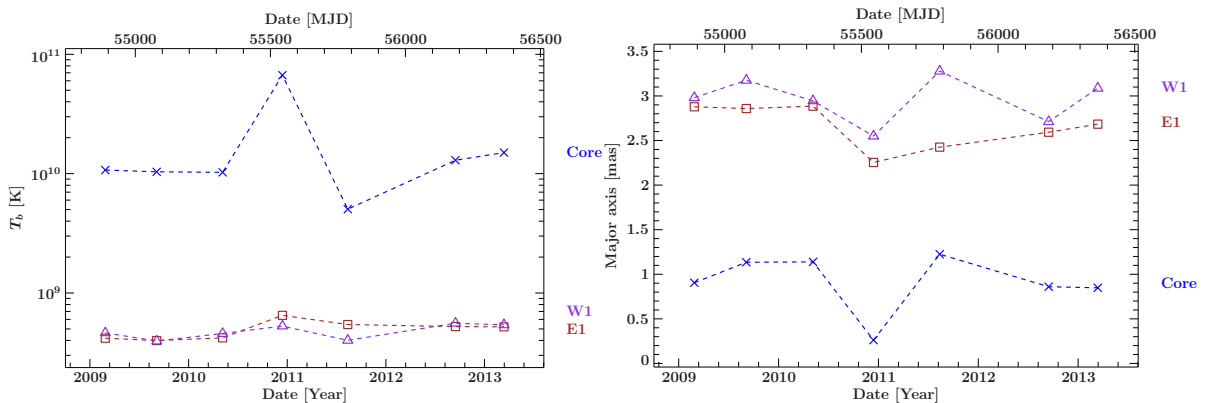


Figure 2.4: Shown are the time evolution of the brightness temperature (left) and major axis (right) of each component. The labels are the same as in Fig. 2.3 The brightness temperature shows no notable variability at about $(4 - 6) \times 10^8$ K for W1 and E1, reflected by small variability of major axis and flux. The core displays high T_b and small major axis for 2010 August, whereas the opposite is the case in 2011.

The components’ speed can be determined by linear regression of either the relative distance to the component set to position zero over time or as a vectorial regression by determining the speeds in both x and y direction separately first and then computing the overall speed. Half of the major axis is taken as an estimate for the positional uncertainty of a component. All computed speeds and their corresponding β_{app} for both redshifts are listed in Table 2.3. The distance over time is plotted in Fig. 2.5 by setting the component core fixed at the origin with both the radial and vectorial fits.

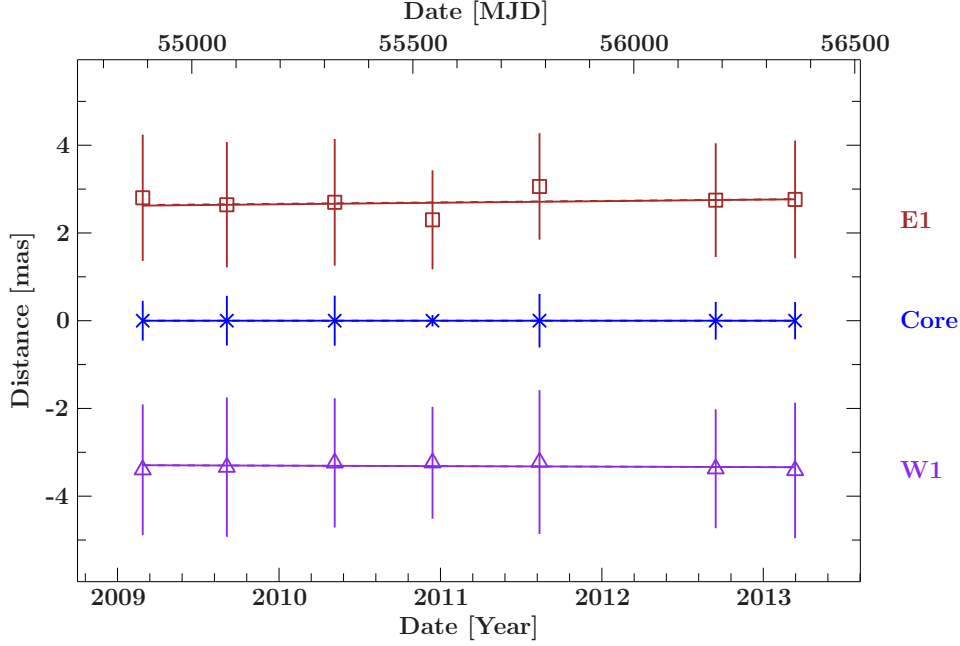


Figure 2.5: Plotted are the component distances relative to the component core over time. The dotted lines represent the linear regression over distance only and the full line represents the vectorial method. The error bars are set to half of the major axis as an estimation of the uncertainties. For both components the lines are practically congruent. All components are stationary within their errors.

Table 2.3: Apparent component speeds relative to the component core in the three component approach

Label	$v_{\text{app}}^{\text{rad a}}$ [mas/yr]	$\beta_{\text{app}}^{\text{rad}}(z_1)^{\text{b}}$	$\beta_{\text{app}}^{\text{rad}}(z_2)^{\text{b}}$	$v_{\text{app}}^{\text{vec a}}$ [mas/yr]	$\beta_{\text{app}}^{\text{vec}}(z_1)^{\text{b}}$	$\beta_{\text{app}}^{\text{vec}}(z_2)^{\text{b}}$
All seven epochs						
W1	-0.011 ± 0.024	0.13 ± 0.28	0.17 ± 0.36	-0.016 ± 0.021	0.19 ± 0.24	0.24 ± 0.31
E1	0.033 ± 0.077	0.38 ± 0.90	0.5 ± 1.2	0.037 ± 0.080	0.43 ± 0.93	0.6 ± 1.2
First five epochs						
W1	-0.075 ± 0.018	0.87 ± 0.21	1.11 ± 0.27	-0.086 ± 0.019	1.00 ± 0.22	1.28 ± 0.29
E1	0.04 ± 0.18	0.5 ± 2.1	0.6 ± 2.7	0.183 ± 0.099	2.1 ± 1.2	2.7 ± 1.5
First three epochs						
W1	-0.1334 ± 0.0088	1.56 ± 0.10	1.98 ± 0.13	-0.1399 ± 0.0089	1.63 ± 0.10	2.08 ± 0.13
E1	-0.08 ± 0.11	0.9 ± 1.3	1.2 ± 1.6	-0.11 ± 0.23	1.3 ± 2.7	1.7 ± 3.4

Note: ^(a) Apparent speed computed by linear regression over distance and time as well as vectorial linear regression.

^(b) Relative apparent speeds $\beta_{\text{app}}^{\text{rad}}$ and $\beta_{\text{app}}^{\text{vec}}$ for both regression methods as well as both redshifts $z_1 = 0.18$ and $z_2 = 0.2321$.

The sign of the speed is defined by Fig. 2.5.

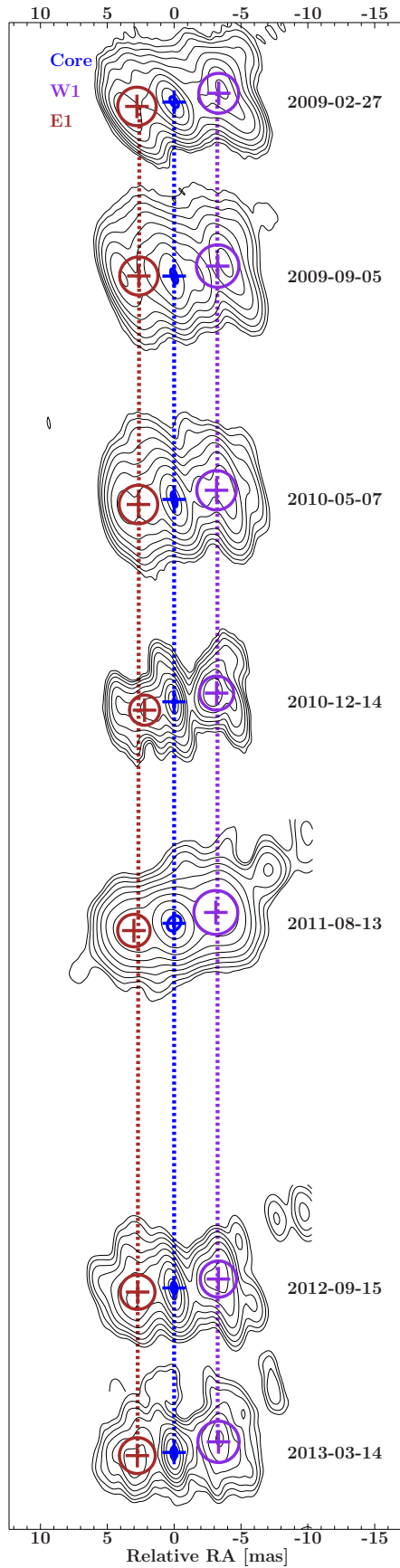


Figure 2.6: Time evolution of the component position for PMN J1603–4904 relative to the central component. Contours are the same as in Fig. 1.7. The clean images are overlaid with the Gaussian model components of the three-component approach (parameters in Table 2.2). The plotted lines are plotted by linear regression. E1 is the eastern component, W1 the western and Core denotes the central component.

2.3 Complex modelfitting

Applying circular and elliptical Gaussians to each of the flux density peaks appearing in the structural map allows one to thoroughly study the jet kinematics of PMN J1603–4904. However it neglects the detailed structure of PMN J1603–4904, especially the extension in the north- and south-western direction. For this reason the two recent epochs were model fitted with more than three components independently. Both models displayed similar features, suggesting the existence of a consistent model for all epochs. Hence the 2012 model was then applied to all other epochs. If it became necessary, certain components were frozen either in their position, their major axis or both. For very small components the size of the major axis was either set to the size of the restoring beam’s minor axis or, if the component was detected in at least another epoch, to the mean value of all other epochs in which the component appears. The resulting models are shown in Fig. 2.10 and parameters are listed in Table 2.2.

The model remains largely the same across all epochs, containing mainly six components. The western region is modelled by a bright component close to where the western component is in the simple model and two components with lower flux density farther from the core in the north- and south-western wings, labelled W2 and W3 respectively. W2 does not appear in the 2011 August observation and would result in a component with negative flux if frozen in position and major axis. This is likely due to the sparse (u, v) -coverage at longer baselines for this epoch making the component unresolvable. The western region can be modeled by two overlapping components, where E1 is the larger component and approximately positioned where the eastern component is in the simple model. The smaller component, E2, has a lower flux density than E1 in all epochs, but coincides within the conventional uncertainties in 2009 September. With the exception of the 2010 December observation, E2 overlaps with or is contained within E1. This exception is likely due to PMN J1603–4904 being resolved better in 2010 December. It is also possible to model the excess flux density in the three recent epochs, however its distance to the core is larger in the 2012 epoch. Finally, in 2013 another component can be detected north of the core. During modelfitting some components would diverge to a major axis of 0 or smaller than the restoring beam’s minor axis. In these cases the minor axis was set to either half of the beam’s minor axis or, in the case of W3, set to the mean of its axes in 2009 February and 2012, since the component was resolved best in these epochs.

Figure 2.7 displays the flux density of all components plotted over time. The core’s flux density evolution is the same as in the simple model within the uncertainties. Qualitatively this is also the case for W1, however all values are slightly lower, but still within the errors. All remaining western components display low flux densities $\lesssim 0.04$ Jy with low variability. Not all the values coincide within the uncertainties which is simply due to an underestimation of the error as all values are close to 0. As E2 and E1 are in close proximity, the flux density within the model is distributed among these components, leading to an overall lower flux density of E1 compared to the simple model. This is

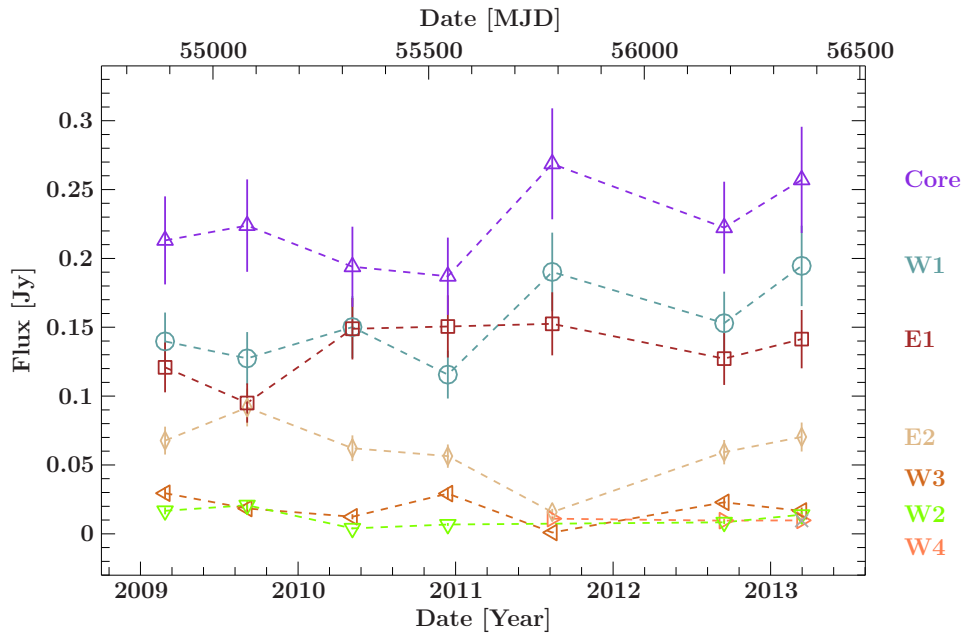


Figure 2.7: Flux density time evolution for all components in the complex model. The flux is mainly contained within the components also apparent in the simple model and close to zero for the remaining components.

especially visible in 2010 September, where their flux densities coincide as noted before. However in 2011 E2 displays a large drop in flux, further showing that this epoch was unable to resolve smaller scale structures due to poor resolution. With the exception of 2010 December and 2011, E1 and E2 show little variability as well.

Looking at the brightness temperature (Fig. 2.8, left), the core, W1 and E1 behave the same as before, where the core emits at $\sim 10^{10}$ K and reaching maximum and minimum values in 2010 September and 2011 due to the epochs' respective resolutions. W1 again shows next to no variability at $\sim 8 \times 10^8$ K however, which is an increase to the simple model. This is due to W1 being smaller in the complex model, but still displaying the same time evolution of the major axis qualitatively. In the complex model W1 does not model the entire western wing anymore, making the component more focused, resulting in a smaller major axis which in return increases its brightness temperature. However E1 now reaches lower values than before within the first three epochs down to $\sim 10^8$ K. As before its major axis shows a large drop between 2010 May and December, but it appears that E1's major axis increases relatively in this model, increasing its major axis more in the first three epochs than in the remaining ones. As such, the drop in size and respective increase in T_b is pronounced more strongly here. E2 displays a similar behaviour as E1 concerning its major axis, especially in 2009 September, reaching its peak size. Due to it being more focussed compared to E1 its brightness temperature is larger than E1's for all but the 2011 epoch, where the flux density of E2 was very low to

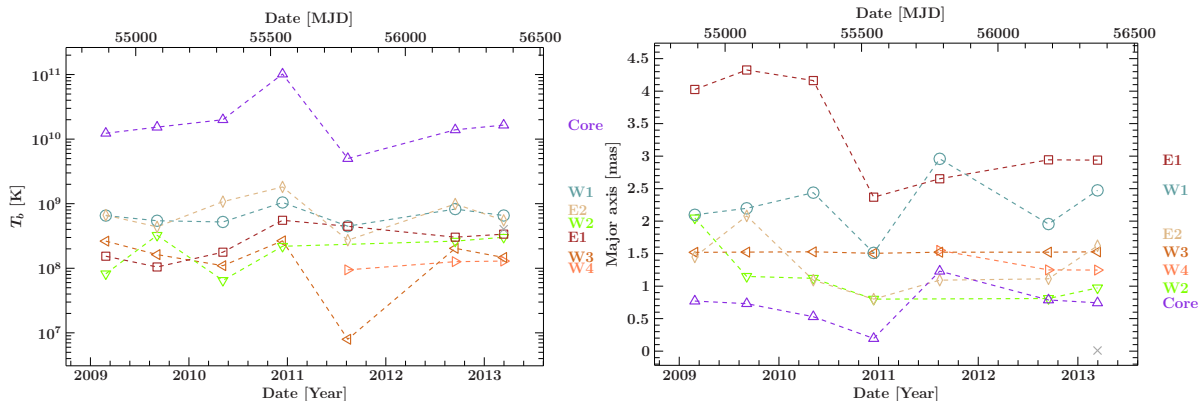


Figure 2.8: Shown are the time evolution of the brightness temperature (left) and major axis (right) of each component in the complex model. The core, W1 and E1 behave largely the same as in the simple model. The other components display a stable behaviour in both T_b and the major axis, where the values of W2 scatter the most.

begin with. The other components are not worth discussing as the major axis was set constant throughout most epochs for them.

Finally, each component's speed may be computed by linear regression. As the components are overall a lot smaller compared to the simple approach, their positions are scattered a lot more which makes a vectorial linear regression unfit with the amount of data available here (see Sect. 3.1). As such, only the linear regression over distance and time is performed. The results are listed in Table 2.4 and the fits are plotted in Fig. 2.9. They will be discussed in Sect. 3.1.

Table 2.4: Linear regression of distance over time in the complex model

Label	$v_{\text{app}}^{\text{a}}$ [mas/yr]	$\beta_{\text{app}}(z_1)^{\text{b}}$	$\beta_{\text{app}}(z_2)^{\text{b}}$
W1	-0.006 ± 0.021	0.07 ± 0.24	0.09 ± 0.31
W2	0.146 ± 0.050	1.71 ± 0.59	2.17 ± 0.75
W3	-0.10 ± 0.14	-1.2 ± 1.6	1.5 ± 2.1
W4	0.7 ± 1.4	8 ± 16	11 ± 21
E1	0.07 ± 0.22	0.8 ± 2.6	1.1 ± 3.3
E2	0.111 ± 0.044	1.30 ± 0.51	1.66 ± 0.65

Note: ^(a) Apparent speed computed by linear regression. ^(b) Apparent speed relative to c for $z_1 = 0.18$ and $z_2 = 0.2321$.

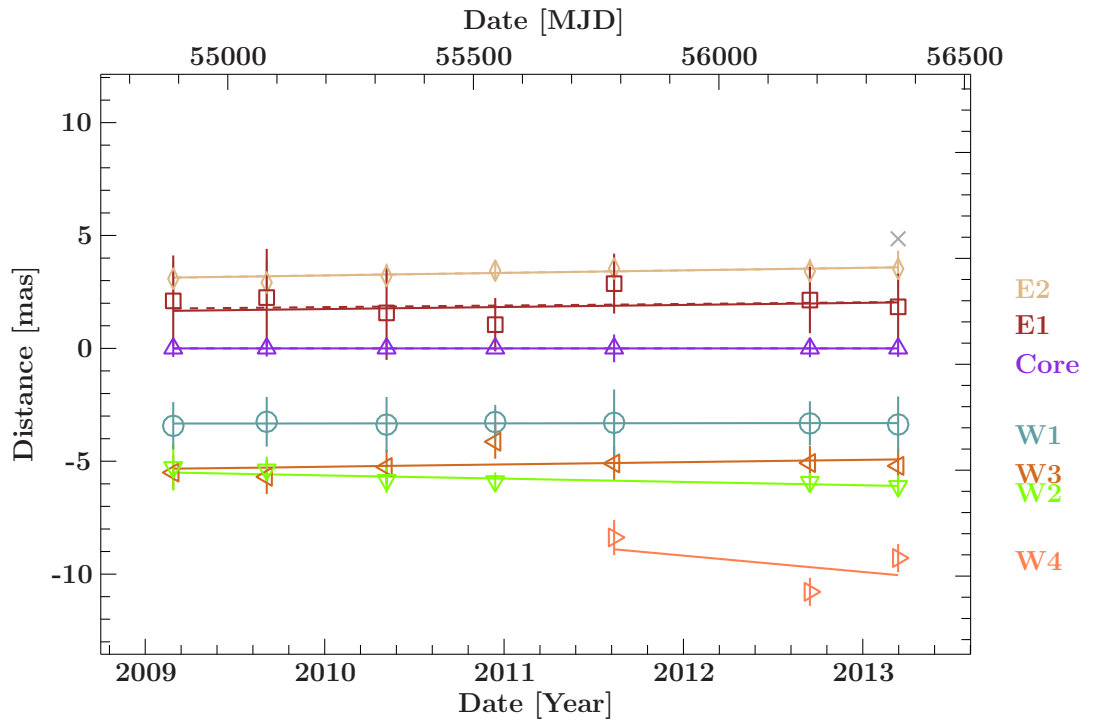


Figure 2.9: Fit by linear regression of the component distances relative to the core in the complex model. The error bars are set to half of the major axis of each component. For the smaller components this is an underestimation of the error, especially visible for W4. Again all components are stationary within their errors.

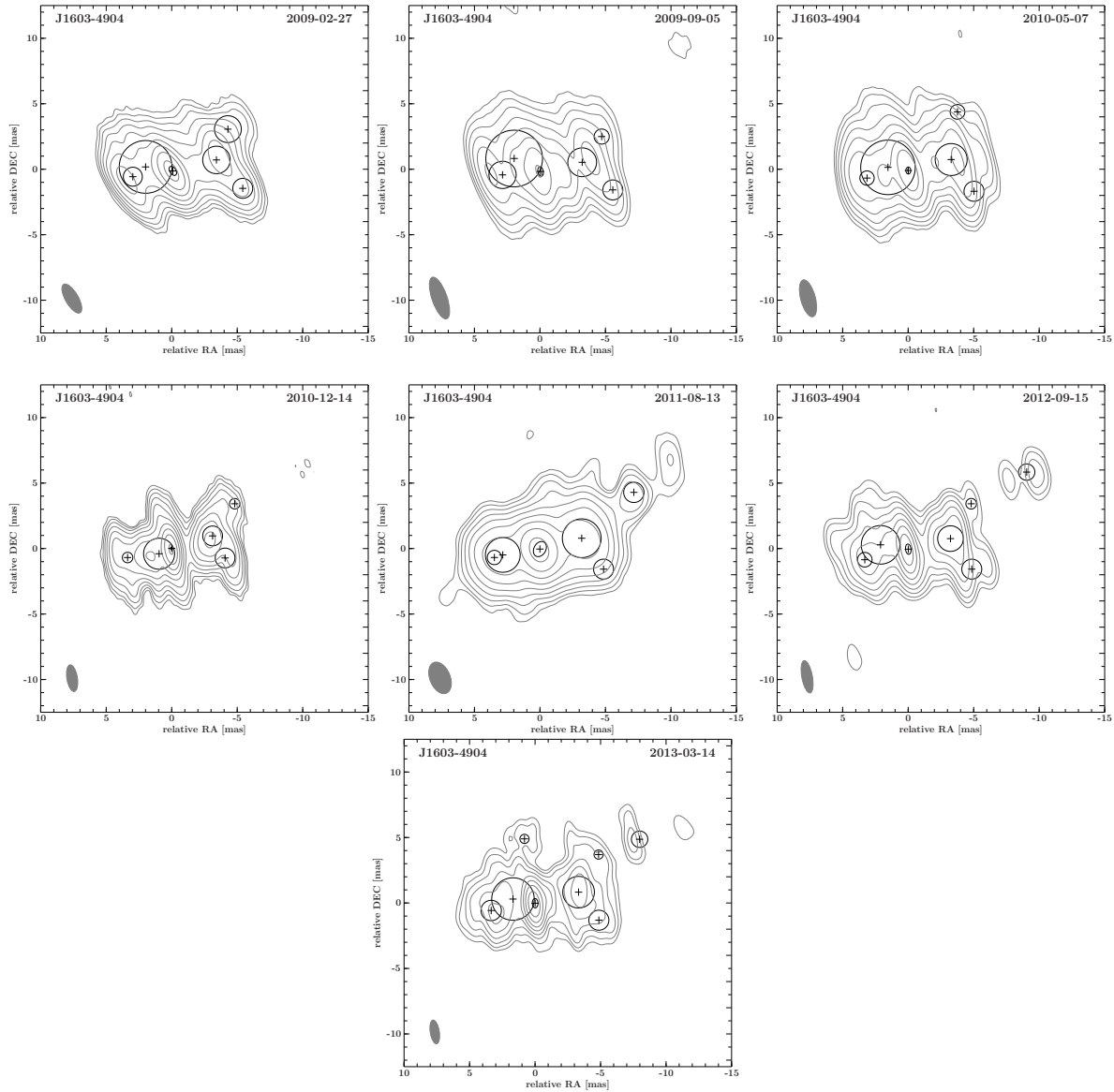


Figure 2.10: Clean maps in gray with model components plotted over them in black. The contours scale logarithmically with a factor of two and the lowest level set to 3σ . The complex model is consistent across all epochs with the 2011 August observation diverging the most. This is likely due to the different resolution and sensitivity compared to the other observations.

Table 2.5: Model fit parameters for the complex model of PMN J1603–4904 at 8.4 GHz

Label	S^a [Jy]	d^b [mas]	θ^b [°]	a_{maj}^c [mas]	a_{min}^c [mas]	P.A. ^c [°]	$(1+z_1)T_b^d$ [10 ⁹ K]	$(1+z_2)T_b^d$ [10 ⁹ K]
2009-02-23/27								
Core	0.213	0.2	-145.4	0.77	0.5	32.2	12.11	12.64
W1	0.140	3.5	-78.2	2.1	2.1	8.6	0.64	0.67
W2	0.017	5.3	-54.5	2.1	2.1	-3.8	0.08	0.08
W3	0.029	5.6	-105.1	1.5	1.5	5.7	0.26	0.27
E1	0.121	2.0	84.9	4.0	4.0	8.4	0.15	0.16
E2	0.068	3.0	100.0	1.5	1.5	5.5	0.65	0.68
2009-09-05								
Core	0.224	0.2	-164.2	0.7	0.4	11.3	15.06	15.73
W1	0.127	3.3	-80.6	2.2	2.2	8.6	0.53	0.56
W2	0.021	5.3	-62.1	1.2 ^e	1.2 ^e	-3.8	0.32	0.33
W3	0.018	5.8	-105.8	1.5 ^e	1.5 ^e	5.7	0.16	0.17
E1	0.095	2.1	67.4	4.3	4.3	8.4	0.10	0.11
E2	0.092	2.9	98.6	2.1	2.1	5.5	0.43	0.45
2010-05-07								
Core	0.194	0.1	-173.1	0.5	0.4	1.2	19.63	20.50
W1	0.150	3.4	-77.3	2.4	2.4	8.6	0.53	0.55
W2	0.004	5.8	-40.7	1.1 ^e	1.1 ^e	-3.8	0.07	0.07
W3	0.012	5.3	-108.5	1.5 ^e	1.5 ^e	5.7	0.11	0.12
E1	0.149	1.5	84.7	4.2	4.2	8.4	0.17	0.18
E2	0.062	3.2	102.1	1.1	1.1	5.5	1.04	1.09
2010-12-14								
Core	0.187	0.0	—	0.2	0.2	4.6	94.65	98.83
W1	0.116	3.3	-72.8	1.5	1.5	8.6	1.04	1.09
W2	0.007	5.9	-54.6	0.8 ^e	0.8 ^e	-3.8	0.21	0.22
W3	0.029	4.1	-100.0	1.5 ^e	1.5 ^e	0.0	0.26	0.27
E1	0.151	1.0	112.3	2.4	2.4	8.4	0.53	0.55
E2	0.056	3.4	101.5	0.8 ^e	0.8 ^e	5.5	1.78	1.86
2011-08-14								
Core	0.269	0.0	—	1.2	0.9	-30.3	4.91	5.13
W1	0.190	3.3	-76.1	3.0	3.0	8.6	0.43	0.45
W3	0.001	5.1 ^e	-108.0 ^e	1.5 ^e	1.5 ^e	5.7	0.01	0.01
W4	0.011	8.4	-59.1	1.6 ^e	1.6 ^e	3.8	0.09	0.09
E1	0.153	2.9	99.7	2.7	2.7	8.4	0.42	0.44
E2	0.016	3.5	101.1	1.1	1.1	5.5	0.26	0.27
2012-09-15								
Core	0.222	0.0	—	0.8	0.4	6.9	13.25	13.84
W1	0.153	3.3	-76.7	2.0	2.0	8.6	0.77	0.81
W2	0.008	5.9 ^e	-54.6 ^e	0.8 ^e	0.8 ^e	-3.8	0.26	0.28
W3	0.023	5.1	-107.9	1.5	1.5	5.7	0.21	0.21
W4	0.010	10.8	-57.2	1.2	1.2	3.8	0.13	0.14
E1	0.127	2.1	82.3	2.9	2.9	8.4	0.31	0.32
E2	0.059	3.4	104.4	1.1	1.1	5.5	0.99	1.04
2013-03-14								
Core	0.257	0.0	—	0.7	0.4	2.2	17.48	18.26
W1	0.188	3.4	-76.0	2.4	2.4	8.6	0.66	0.69
W2	0.013	6.1	-52.7	0.7 ^e	0.7 ^e	7.1	0.56	0.58
W3	0.018	5.0	-105.1	1.5 ^e	1.5 ^e	5.7	0.16	0.16
W4	0.010	9.3	-58.6	1.3 ^e	1.3 ^e	3.8	0.12	0.12
E1	0.143	1.7	79.9	3.2	3.2	8.4	0.28	0.30
E2	0.076	3.4	99.7	1.6	1.6	5.5	0.60	0.62
E3	0.008	5.0	9.4	0.7 ^e	0.7 ^e	7.1	0.34	0.35

Note: ^(a) Integrated flux density of the model component. ^(b) Distance and position angle of the component from the phase center. ^(c) Major and minor axes of the component and position angle of the major axis. ^(d) Corrected brightness temperature with $z_1 = 0.18$ and $z_2 = 0.2321$. ^(e) The marked values were set as constant for the algorithm to reach a conclusive model.

3 Discussion

3.1 Orientation and kinematics of the jet system

In this section the results from Sections 2.1 through 2.3 are used to determine the inclination angle ϕ as well as the components' speed with further discussion.

Solving equation 1.1.10 for ϕ yields the relation

$$\phi = \arccos \left[\frac{1 \left(\frac{S_{\text{jet}}}{S_{\text{counter}}} \right)^{\frac{1}{3-\alpha}} - 1}{\beta \left(\frac{S_{\text{jet}}}{S_{\text{counter}}} \right)^{\frac{1}{3-\alpha}} + 1} \right] \quad (3.1.1)$$

which, taking the limit $\beta \rightarrow 1$, gives an upper limit for ϕ . For the flux densities of jet and counterjet the values of eastern and western components given by the model (Table 2.2) are used, where the assumption is made that these regions can be described as a jet to counterjet system with the central region as the core. As both the jet and counterjet are described by only one spherical Gaussian, $3 - \alpha$ is used as an exponent. The ratio R of jet to counterjet flux is determined by taking the mean over all epochs, which results in $R = 1.21 \pm 0.05$. α is taken to be between -2 and -1 (Müller, Kadler, et al., 2014), however the computed values differ only marginally and agree within the standard error. This yields an upper limit of $\phi < 89^\circ$, suggesting that PMN J1603–4904 is an edge-on system. This is further supported by the fact that within the $15 - 20\%$ error the flux densities of eastern and western component coincide for all epochs, i.e. next to no beaming effects are present. In Müller, Kadler, et al. (2014) a pattern speed of $\beta \approx 0.25$ of the source NGC 1052 (Vermeulen, Ros, Kellermann, et al., 2003) and $\alpha = -0.5$, i.e. optically thin emission, were used to determine ϕ . Using these values, this yields an angle of $\phi \sim 84^\circ$, which is consistent with the value derived in Müller, Kadler, et al. (2014). It is unlikely that ϕ is smaller as both β and α are rather conservative assumptions, yielding $84^\circ < \phi < 89^\circ$.

The speeds resulting from linear regression in the simple model and their corresponding β_{app} for both redshifts are listed in Table 2.3. The distance over time is plotted in Fig. 2.5. Looking at absolute values the vectorial fit yields a slightly larger speed in all cases and is generally more accurate due to consisting of the linear regressions in both x- and y-direction, reflected by a smaller relative error in all cases. Additionally linear regression was performed with only the first five and the first three epochs relative to the component core (Table 2.3). In both cases the uncertainties for W1 are lower than

for all 7 epochs, thus reaching unphysically high values for β , which is assumed to be approximately the same as β_{app} as PMN J1603–4904 is likely an edge-on system (see Sect. 2.1). The small error is likely due to the small statistical scattering of the values, resulting in an underestimation of the error by calculation only. It should be also noted that the vectorial fit for E1 when using data of the first five epochs yields an unphysically high value as well. This is likely due to the fact that, while distance can remain largely the same, the x- and y-positions of each component can differ on a larger scale, resulting in an overall higher speed and underestimation of the error. However these changes in x- and y-position are likely due to different array configurations and e.g. differences in window placements during imaging. These statistical uncertainties can only be removed with a sufficient amount of data, which is the case for all seven epochs as the values coincide well. The computed fits for the first three epochs are consistent with Müller, Kadler, et al. (2014). For the first five epochs only E1 yields the same value as Müller (2014), while the speed for W1 is slightly lower, but coincides within the error with Müller (2014). Using the distance fit of E1 an upper limit of $|v_{\text{app,old}}| < 0.2 \text{ mas/yr}$ can be determined in both cases. The new data improves this limit significantly, giving the result

$$|v_{\text{app}}| < 0.11 \frac{\text{mas}}{\text{yr}} . \quad (3.1.2)$$

In the likely case of an edge-on system this limit would lead to an intrinsic speed of $\beta > 1$ for both redshifts, meaning that more data is needed to reduce the uncertainties and determine the real speed. It should also be noted that both components are stationary within their errors, which likely means that the jets are moving rather slowly, supported by the low values computed for W1. Additionally the relative motion of E1 and W1 can be constrained to $|v_{\text{app}}^{\text{rel}}| < 0.13 \text{ mas/yr}$ or $\beta_{\text{app}}^{\text{rel}} < 2.0$ at $z = 0.2321$.

The speeds in the complex model are listed in Table 2.4 and the distance over time plot is shown in Fig. 2.9. As the uncertainty is taken to be the semi-major axis, the uncertainties are underestimated for the smaller components, most notably W4, where the amount of scattering exceeds the error bars and linear regression yields absurdly high values. However the results for W1 and E1 coincide well with the results from the simple model. Since E1 has a larger major axis in all epochs in the complex model, its speed yields a larger error as well compared to the simple model. Yet again all components are stationary within their errors, showing that the jets of PMN J1603–4904 are likely slow moving.

The details of this complex model further supports the central component as being the designated core of PMNJ160–4904 since both the eastern and western wings can be modeled with more than one component, whereas the central region contains one small and bright elliptical component in both models. Both its wings are far from being simple blobs, i.e. spherical Gaussians. Hence they can be approximated better by using several spherical Gaussians placed along special features within its contours. Due to the large similarities between the components appearing in both models it can be concluded that the complex approach describes the detailed structure of PMN J1603–4904.

3.2 Implications for the classification of PMN J1603–4904

Based on the available data, a classification of PMN J1603–4904 is no easy task. It has been classified as a BL Lac type object based on its lack of emission lines and multiwavelength properties (Nolan, Abdo, et al., 2012), however its low variability and mas-scale structures strongly challenge this classification and suggest other scenarios, most notably PMN J1603–4904 being a Compact Symmetric Object (CSO). In this section I will summarize the argumentation for the likeliest classification scenarios given in Müller (2014) within the context of the recent optical data (Goldoni, Pita, et al., 2015) and the new VLBI data shown in the previous sections.

As explained in Sect. 1.1.1, BL Lac objects show high variability across the entire electromagnetic spectrum on all timescales. They lack optical and infrared features due to strong non-thermal emission from the jets and display a high degree of polarization ($\sim 10\%$). Due to their small inclination angle, the jets seemingly undergo superluminal motion. No short-term variability has been detected for PMN J1603–4904 by neither *Fermi*/LAT (Nolan, Abdo, et al., 2012) nor within the ATCA light curve over a course of four years (Fig. 1.8). Only low-level long time-variability at ≥ 10 GeV was detected (Ackermann, Ajello, Allafort, et al., 2013) and confirmed after four years of observation with *Fermi*. With 7 epochs of VLBI data no structural variability on mas-scale could be detected. The flux density at 8.4 GHz remains stable for all components in both the simple and complex models within the uncertainties (Fig. 2.3 and Fig. 2.7). The kinematic analysis yields no superluminal motion and even gives the possibility of stationary components within errors (Fig. 2.5 and Fig. 2.9). Observations by Murphy, Sadler, Ekers, et al. (2010) give an upper limit of $< 1.2\%$ at 20 GHz and $< 1\%$ at 8.4 GHz for its degree of polarization which is well below the expectation for BL Lacs. In Müller (2014) the SED of PMN J1603–4904 shows a strong excess in infrared and Compton dominance, which is unusual for BL Lac objects. The existence of optical emission lines further challenges this scenario especially as their equivalent width exceeds the limit for BL Lacs (Goldoni, Pita, et al., 2015). Finally, the structure of PMN J1603–4904 at 8.4 GHz is very unusual for a BL Lac object. Usually they display a one-sided jet with a bright, optically thick core at its end extending conically along the jet axis, whereas PMN J1603–4904 has a symmetric structure with a bright, small core at the center and the eastern and western wings in both models. All brightness temperatures are $< (2 \times 10^{10})$ K (with the exception of one value at 10^{11} K, Fig. 2.4 and Fig. 2.8), which is significantly lower than usually observed for beamed emission of BL Lacs (Ojha, Kadler, et al., 2010). All these aspects challenge the classification of PMN J1603–4904 as a BL Lac object which leads to the necessity of different classification scenarios of which PMN J1603–4904 being a Compact Symmetric Object (CSO) is a very likely possibility.

CSOs show a distinct symmetric, double shaped structure on small scales and are assumed to be radio galaxies in their earliest stages of development viewed under a large

inclination angle (see Sect. 1.1). Little to no motion is detected for single jet components. These objects display low radio variability ($\lesssim 10\%$) and low polarization ($\leq 1\%$) as well as a steep spectrum with a flat center and an intensity ratio of less than 10:1. The mas-scale structure of PMN J1603–4904 agrees very well with the given criteria for CSOs. It displays a bright, compact component in the center with a flat spectrum ($\alpha = -0.4$, Müller, Kadler, et al., 2014) and two lobes to the west and east with steeper spectra. Usually cores of CSOs are fainter and the spectrum is dominated by the side lobes, however the center is the brightest feature of PMN J1603–4904, flattening its overall spectrum (Müller, 2014). Sokolovsky, Y. Y. Kovalev, et al. (2011) give a mean value to the brightness temperature of $T_{b,\text{mean}} \sim 10^9$ K for CSOs which is consistent with the data on PMN J1603–4904 for all epochs, as well as a mean index for CSOs of $\alpha_{\text{mean}} = -0.52$ (between 2.3 GHz and 8.4 GHz), consistent with Müller, Kadler, et al. (2014). Additionally PMN J1603–4904 displays no notable variability at 8.4 GHz. Even with data of two new epochs, no significant motion relative to the central component could be detected. The upper limit to the jet speed could be reduced however. This means that the kinematic age of PMN J1603–4904 has yet to be determined and a two-sided motion is not proven yet. In Section 2.1 the ratio of the flux density of the two lobes, viewed as a jet and counterjet system, yielded $R = 1.21 \pm 0.05$, consistent with the value given in Müller (2014). Here a pattern speed of $\beta \approx 0.25$ of the source NGC 1052 (Vermeulen, Ros, Kellermann, et al., 2003) and $\alpha = -0.5$, i.e. optically thin emission, was used. With Equation 3.1.1 this yields $\phi \sim 84^\circ$, again consistent with Müller (2014), supporting the fact that PMN J1603–4904 is an edge-on system. The VLBI images at 8.4 GHz show a structure with a highest extension of ~ 15 mas. This corresponds to a projected size of ~ 64 pc at a redshift of $z = 0.18$ and ~ 84 pc at $z = 0.2321$. ATCA observations (Müller, 2014) limit the overall structure of PMN J1603–4904 to $\sim 1'$, corresponding to ~ 3 kpc at $z = 0.18$. With this maximum extension however no distinction between a CSO and a small radio galaxy can be made. Properties in the X-rays shown by Müller (2014) further suggest a classification other than the BL Lac scenario, pointing towards alternatives. With the above given properties PMN J1603–4904 could very well be a classified as a CSO. However if this were the case, PMN J1603–4904 would be the first CSO to display strong γ -ray emission.

In Müller (2014) other scenarios were also suggested, namely PMN J1603–4904 being a Galactic source and a symmetric structure caused by gravitational lensing, which were however deemed unlikely and hence dismissed. Another explanation is found in PMN J1603–4904 being a starburst galaxy due to its broadband emission properties. However it would be the most luminous γ -ray loud starburst galaxy.

4 Summary and Outlook

In this work two new VLBI epochs at 8.4GHz of the unusual γ -ray source PMN J1603–4904 from the TANAMI sample were imaged and modeled. The new images are consistent with the previous five epochs. The structure of PMN J1603–4904 consists of a compact, bright center and two lobes extending to the east and west.

The structure could be modeled with three components set to the eastern, western and central flux density peaks. It shows no flux variability within conventional uncertainties and brightness temperatures well below the Compton limit of 10^{12} K. Due to its spectral properties, the central component is the best candidate for the source’s core. The flux ratio of the two lobes averages to about $R \approx 1.21$ and yields an inclination angle of $84^\circ < \phi < 89^\circ$, suggesting that the source is an edge-on system.

With positional data from seven epochs of observations linear regression gives an upper limit of $|v_{\text{app}}| < 0.11$ mas/yr, which is a clear improvement to the previous limit of $|v_{\text{app}}| < 0.2$ mas/yr. However no significant motion could be detected as all components are stationary within their errors even if the speed is computed relative to each of the other components.

A complex model containing seven components was found for the 2012 epochs and applied to the other observations. The model stays consistent throughout all epochs with only little necessity to freeze single components. The kinematic analysis again yields no significant variability of flux density and brightness temperature as well as no significant motion, consistent with the simple model. Due to the similarities, both models describe the source equivalently, where the simple approach focuses on the brightest features and represents the respective lobes, whereas the complex model describes the detailed structure of each lobe better than a singular Gaussian.

The classification of PMN J1603–4904 was discussed, adopting the argumentation of Müller (2014). The traditional BL Lac scenario can be ruled out due to the mas-scale properties of PMN J1603–4904 and the existence of optical emission lines (Goldoni, Pita, et al., 2015). Hence a classification as a CSO, i.e. a young radio galaxy, is a more likely alternative, but cannot be fully confirmed.

Future VLBI observations will help to further restrain the upper limit to the jet speed and allow to prove or disprove a two sided motion. This will also allow determining the kinematic age of PMN J1603–4904, which will help test the classification as a CSO. Future analysis of data from the Giant Metrewave Radio Telescope (GMRT) of frequencies below 1 GHz will allow to determine the $\tau = 1$ turnover frequency of PMN J1603–4904. This will allow us to further constrain the extension of the source, possibly ruling out a scenario as a small radio galaxy and classifying it as a CSO.

Acknowledgments

First of all, I would like to thank my advisor Prof. Dr. Matthias Kadler for giving me the opportunity to work in this field of astronomy, especially for enabling me to work on such an interesting topic. The meetings and discussions with him as well as his feedback greatly helped improve the results and quality of this thesis and his lectures on astronomy motivated me to work in this field.

In addition I would like to thank the chair of astronomy, with Prof. Dr. Karl Mannheim as its holder, for their cheerful attitude and warm welcoming of new members.

I would also like to thank Dr. Cornelia Müller, who previously worked on PMN J1603–4904. Without these previous results, this work could not have happened. Her feedback was of great help to improve this work and eliminate errors.

Next, I would like to thank Robert Schulz and Jonas Trüstedt whom I could always contact during the analysis process. I highly appreciate all advice I received during crucial parts of my calculations.

Furthemore I'd like to thank all members of the TANAMI project for providing the data used in this thesis as well as its a priori calibration and especially Dr. Roopesh Ojha for his coordination., who, together with Prof. Dr. Matthias Kadler, is head of the project.

I want to thank my colleagues in the Bachelor's office for creating a nice working atmosphere, where everyone is readily available to help each other out with smaller problems.

Finally, I would like to thank my family for their great confidence and support.

This research has made use of the Interactive Spectral Interpretation System (ISIS) (Houck and Denicola, 2000)

This research has made use of a collection of ISIS scripts provided by the Dr. Karl Remeis observatory, Bamberg, Germany at <http://www.sternwarte.uni-erlangen.de/isis/>

Bibliography

- Abdo, A. A., M. Ackermann, M. Ajello, et al. (2010). *The Astrophysical Journal* 188.
- Ackermann, M. et al. (2015). “The Third Catalog of Active Galactic Nuclei Detected by the Fermi Large Area Telescope”. *The Astrophysical Journal* 810, 14, p. 14. DOI: 10.1088/0004-637X/810/1/14. arXiv: 1501.06054 [astro-ph.HE].
- Ackermann, M., M. Ajello, A. Allafort, et al. (2013). *The Astrophysical Journal Supplement* 209.
- An, T. and W. A. Baan (2012). “The Dynamic Evolution of Young Extragalactic Radio Sources”. *The Astrophysical Journal* 760.1, p. 77.
- Antonucci, R. (1993). “Unified models for active galactic nuclei and quasars”. *Annual review of astronomy and astrophysics* 31, pp. 473–521.
- Augusto, P., J. I. Gonzalez-Serrano, et al. (2006). “Flat-spectrum symmetric objects with ~ 1 kpc sizes - I. The candidates”. *Monthly Notices of the Royal Astronomical Society* 368, pp. 1411–1428. DOI: 10.1111/j.1365-2966.2006.10227.x. eprint: astro-ph/0602511.
- Burke, B. F. and F. Graham-Smith (2010). *An introduction to radio astronomy*. 3. ed. Cambridge Univ. Press.
- Chen, P. S. and H. G. Shan (2011). “Infrared Spectral Observation of Eight BL Lac Objects from the Spitzer Infrared Spectrograph”. *The Astrophysical Journal* 732.1, p. 22.
- Cotton, W. D. (1995). *Very Long Baseline Interferometry and the VLBA*. Ed. by J. A. Zensus, P. J. Diamond, and P. J. Napier. Vol. 82. Astronomical Society of the Pacific Conference Series.
- Diamond, P. J. (1995). *Very Long Baseline Interferometry and the VLBA*. Ed. by J. A. Zensus, P. J. Diamond, and P. J. Napier. Vol. 82. Astronomical Society of the Pacific Conference Series.
- Donato, D., G. Ghisellini, et al. (2001). “Hard X-ray properties of blazars”. *Astronomy and Astrophysics* 375, pp. 739–751. DOI: 10.1051/0004-6361:20010675. eprint: astro-ph/0105203.
- Fanaroff, B. L. and J. M. Riley (1974). “The morphology of extragalactic radio sources of high and low luminosity”. *Monthly Notices of the Royal Astronomical Society* 167, 31P–36P.
- Fassnacht, C. D. and G. B. Taylor (2001). *The Astronomical Journal* 122.
- “Very Long Baseline Interferometry: Techniques and Applications; ; [proceedings of the NATO Advanced Study Institute on the Techniques and Applications of Very Long Baseline Interferometry, Castel S. Pietro Terme, Bologna, Italy, September 12 - 23,

- 1988]” (1989). Ed. by M. Felli and R. Spencer. NATO ASI series : Ser. C, Mathematical and physical sciences ; 283. Kluwer.
- Goldoni, P., S. Pita, et al. (2015). “Optical-NIR spectroscopy of the puzzling gamma-ray source 3FGL 1603.9-4903/PMN J1603-4904 with X-shooter”. *Astronomy and Astrophysics*. arXiv: 1510.06234 [astro-ph.HE].
- Greisen, E. W. (2003). “AIPS, the VLA, and the VLBA”. *Information Handling in Astronomy - Historical Vistas* 285, p. 109. DOI: 10.1007/0-306-48080-8_7.
- Högbom, J. A. (1974). “Aperture Synthesis with a Non-Regular Distribution of Interferometer Baselines”. *Astronomy and Astrophysics Supplement* 15, p. 417.
- Houck, J. C. and L. A. Denicola (2000). “ISIS: An Interactive Spectral Interpretation System for High Resolution X-Ray Spectroscopy”. *Astronomical Data Analysis Software and Systems IX*. Ed. by N. Manset, C. Veillet, and D. Crabtree. Vol. 216. Astronomical Society of the Pacific Conference Series, p. 591.
- Jansen, F., D. Lumb, et al. (2001). “XMM-Newton observatory. I. The spacecraft and operations”. *Astronomy and Astrophysics* 365, pp. L1–L6. DOI: 10.1051/0004-6361:20000036.
- Kadler, M., R. Ojha, and TANAMI Collaboration (2015). “TANAMI: Multiwavelength and multimessenger observations of active galaxies”. *Astronomische Nachrichten* 336, p. 499. DOI: 10.1002/asna.201512186. arXiv: 1506.03947 [astro-ph.HE].
- Kellermann, K. I., R. Sramek, et al. (1989), p. 1195.
- Kellermann, K. I., M. L. Lister, D. C. Homan, et al. (2004). *The Astrophysical Journal* 609.
- Kembhavi, A. K. and J. V. Narlika (1999). *Quasars and Active Galactic Nuclei: An Introduction*. Cambridge University Press.
- Kovalev, Y. Y. et al. (2005). “Sub-milliarcsecond imaging of quasars and active galactic nuclei. 4. Fine scale structure”. *Astron. J.* 130, pp. 2473–2505. DOI: 10.1086/497430. arXiv: astro-ph/0505536.
- Koyama, K., H. Tsunemi, et al. (2007). “X-Ray Imaging Spectrometer (XIS) on Board Suzaku”. *Publications of the Astronomical Society of Japan* 59, pp. 23–33. DOI: 10.1093/pasj/59.sp1.S23.
- Levenberg, K. (1944). “A Method for the Solution of Certain Non-Linear Problems in Least Squares”. *Quarterly of Applied Mathematics* 2, p. 164.
- Lister, M. L. and D. C. Homan (2005). *The Astronomical Journal* 130.
- Müller, C. (2014). “High-Resolution Observations of Active Galactic Nuclei in the Southern Hemisphere”. PhD thesis. Institut für Physik und Astronomie, Julius-Maximilians-Universität Würzburg.
- Müller, C. et al. (2015). “Redshifted Fe K α line from the unusual γ -ray source PMN J1603-4904”. *Astronomy and Astrophysics* 574, A117, A117. DOI: 10.1051/0004-6361/201425442. arXiv: 1501.00790 [astro-ph.HE].
- Müller, C., M. Kadler, et al. (2014). “The unusual multiwavelength properties of the gamma-ray source PMN J1603-4904”. *Astronomy and Astrophysics* 562, A4, A4. DOI: 10.1051/0004-6361/201322827. arXiv: 1312.4827 [astro-ph.HE].

-
- Murphy, T., E. M. Sadler, R. D. Ekers, et al. (2010). *Monthly Notices of the Royal Astronomical Society* 402.
- Nolan, P. L., A. A. Abdo, et al. (2012). “Fermi Large Area Telescope Second Source Catalog”. *The Astrophysical Journal Supplement* 199, 31, p. 31. arXiv: 1108.1435 [astro-ph.HE].
- Ojha, R., M. Kadler, et al. (2010). “TANAMI: tracking active galactic nuclei with austral milliarcsecond interferometry . I. First-epoch 8.4 GHz images”. *Astronomy and Astrophysics* 519, A45, A45. DOI: 10.1051/0004-6361/200912724. arXiv: 1005.4432.
- Peck, A. B. and G. B. Taylor (2000). *The Astrophysical Journal* 534.
- Rybicki, G. B. and A. P. Lightman (1979). *Radiative processes in astrophysics*. A Wiley-Interscience publication. Wiley.
- Seyfert, C. K. (1943). “Nuclear Emission in Spiral Nebulae”. *The Astrophysical Journal* 97, p. 28. DOI: 10.1086/144488.
- Sokolovsky, K. V., Y. Y. Kovalev, et al. (2011). “VLBI-selected sample of compact symmetric object candidates and frequency-dependent position of hotspots”. *Astronomy and Astrophysics* 535, A24, A24. DOI: 10.1051/0004-6361/201015772. arXiv: 1107.0719 [astro-ph.CO].
- Stevens, J., P. G. Edwards, R. Ojha, et al. (2012). *Proceedings of Fermi and Jansky: Our Evolving Understanding of AGNs*. Ed. by R. Ojha, D. Thompson, and C. Dermer.
- Thompson, A. R., J. M. Moran, and G. W. Swenson (2001). *Interferometry and synthesis in radio astronomy*. New York: Wiley.
- Urry, C. M. and P. Padovani (1995). “Unified Schemes for Radio-Loud Active Galactic Nuclei”. *Publications of the Astronomical Society of the Pacific* 107, p. 803. DOI: 10.1086/133630. eprint: astro-ph/9506063.
- Vermeulen, R. C., E. Ros, K. I. Kellermann, et al. (2003). *Astronomy and Astrophysics* 401.
- Vernet, J., H. Dekker, et al. (2011). “X-shooter, the new wide band intermediate resolution spectrograph at the ESO Very Large Telescope”. *Astronomy and Astrophysics* 536, A105, A105. DOI: 10.1051/0004-6361/201117752. arXiv: 1110.1944 [astro-ph.IM].

Selbstständigkeitserklärung

Ich versichere, die vorliegende Arbeit nach allgemeiner Studien- und Prüfungsordnung für die Bachelor- und Masterstudiengänge (ASPO) an der Julius-Maximilians-Universität Würzburg selbstständig verfasst und keine anderen als die angegebenen Quellen und Hilfsmittel benutzt, sowie noch keiner anderen Prüfungsbehörde zur Erlangung eines akademischen Grades vorgelegt zu haben.

Würzburg, den 10. Dezember 2015

Amar Hekalo